ETH zürich

ETH Library

CO2-free conversion of CH4 to syngas using chemical looping

Journal Article

Author(s):
Donat, Felix; Müller, Christoph R.

Publication date:
2020-12-05

Permanent link:
https://doi.org/10.3929/ethz-b-000427820

Rights / license:
Creative Commons Attribution 4.0 International

Originally published in:
Applied Catalysis B: Environmental 278, https://doi.org/10.1016/j.apcatb.2020.119328

This page was generated automatically upon download from the ETH Zurich Research Collection.
For more information, please consult the Terms of use.

Applied Catalysis B: Environmental 278 (2020) 119328

Contents lists available at ScienceDirect

Applied Catalysis B: Environmental

journal homepage: www.elsevier.com/locate/apcatb

CO_2-free conversion of CH_4 to syngas using chemical looping

Felix Donat*, Christoph R. Müller*

Laboratory of Energy Science and Engineering, Department of Mechanical and Process Engineering, ETH Zürich, Leonhardstrasse 21, 8092 Zürich, Switzerland

ARTICLE INFO

Keywords:
Partial oxidation
Methane reforming
Water splitting
Chemical looping
Oxygen carrier

ABSTRACT

Chemical looping can provide attractive alternative process routes in which solid oxygen carriers function as lattice oxygen transfer agents, for example for the partial oxidation of methane. We report on the development of a perovskite-based oxygen carrier ($La_{0.85}Sr_{0.15}Fe_{0.95}Al_{0.05}O_{3-\delta}$) that enables the complete conversion of CH_4 to a synthesis gas (a mixture of H_2 and CO, selectivity > 99 %) through donation of its lattice oxygen (up to 9 wt%) at temperatures > 900 °C. The thermodynamic properties of the oxygen carrier permit its lattice oxygen to be replenished with CO_2 or H_2O, of which > 94 % is converted into CO or H_2, respectively. The potential of this compositionally and structurally flexible oxygen carrier is demonstrated in a continuous experiment lasting more than 45 days (~ 4050 redox cycles), in which all CH_4 (reductant) and all CO_2 (oxidant) is converted into a synthesis gas without CO_2 contamination.

1. Introduction

Metal oxides that function as oxygen reservoirs have shown to possess high potential for process intensification and emission reduction in hydrocarbon conversion processes [1,2]. One such process is the partial oxidation of CH_4 (POx; $CH_4 + 0.5\ O_2 \rightarrow CO + 2\ H_2$), which requires gaseous O_2 under the conventional scheme. The theoretical ratio of H_2/CO in the synthesis gas produced is two, which is suitable for methanol or for Fischer-Tropsch processes to produce liquid hydrocarbons and synthetic fuels [3–6]. The POx reaction can be realized with lattice oxygen derived from a metal oxide instead of gaseous O_2 and thereby eliminate the energy consumptions associated with the cryogenic production of O_2 [7]. Redox-active lattice oxygen that has been removed from the metal oxide is replenished in a second reaction step using an oxidant such as air. The two-step reaction scheme is illustrated in Reactions 1 and 2, where MeO_x and MeO_{x-1} denote the oxidized and reduced states of the metal oxide; note that the two do not necessarily need to be structurally similar and can be composed of multiple phases.

$$CH_4 + MeO_x \rightarrow CO + 2\ H_2 + MeO_{x-1} \quad (1)$$

$$0.5\ O_2 + MeO_{x-1} \rightarrow MeO_x \quad (2)$$

Adding Reactions 1 and 2 yields the conventional POx and the same heat of reaction (-23 kJ mol^{-1} at 900 °C). Metal oxide-mediated redox reactions have been termed chemical looping (CL), and the metal oxides function as oxygen carriers. The majority of research in chemical looping has dealt with the total oxidation of hydrocarbon feedstocks for power generation with inherent CO_2 capture [8–11]. Whether an oxygen carrier is suitable for Reaction 1 or not depends solely on its thermodynamic properties and the equivalent equilibrium partial pressure of oxygen (p_{O2}) under which it transitions between two oxidation states [12]. The range of p_{O2} enabling the partial oxidation of CH_4 is orders of magnitude lower than that of the p_{O2} required to totally oxidize CH_4, which also implies that a re-oxidation of the reduced oxygen carrier is thermodynamically feasible using oxidants with a much lower oxidation potential than air in Reaction 2, e.g. CO_2 or H_2O (Reactions 3 and 4).

$$CO_2 + MeO_{x-1} \rightarrow CO + MeO_x \quad (3)$$

$$H_2O + MeO_{x-1} \rightarrow 2\ H_2 + MeO_x \quad (4)$$

Thus, the combination of Reactions 1 and 3 or 4 has also been referred to as the CL dry reforming of CH_4 or the CL steam reforming of CH_4, depending on the oxidant (or mixtures of oxidants) used and the ratio of H_2/CO produced over an entire redox cycle (dry reforming: $CH_4 + CO_2 \rightarrow 2\ CO + 2\ H_2$; steam reforming: $CH_4 + H_2O \rightarrow CO + 3\ H_2$).

Iron oxide-based oxygen carriers can partially oxidize CH_4 efficiently, provided their oxidation states (when performing Reactions 1 and 2/3/4 cyclically) are controlled precisely in the process such that the total oxidation of CH_4 ($CH_4 + 4\ MeO_x \rightarrow CO_2 + 2\ H_2O + 4\ MeO_{x-1}$) is avoided [13–15]. Structural modifications [16] or doping of the iron oxide-based oxygen carrier with yttrium [17] or cobalt [18] were found to improve the selectivity towards CO. Recently, perovskites or

* Corresponding authors.
E-mail addresses: donat@ethz.ch (F. Donat), muelchri@ethz.ch (C.R. Müller).

https://doi.org/10.1016/j.apcatb.2020.119328
Received 29 May 2020; Received in revised form 1 July 2020; Accepted 8 July 2020
Available online 10 July 2020
0926-3373/ © 2020 The Authors. Published by Elsevier B.V. This is an open access article under the CC BY license (http://creativecommons.org/licenses/by/4.0/).

related oxygen-deficient structures have attracted significant attention, as their compositional and structural flexibility allows tuning their thermodynamic properties such that a high selectivity towards synthesis gas is obtained. Perovskites enjoy popularity in many different areas owing to their high, mixed electronic and ionic conductivities, e.g. as a component of solid oxide fuel cells [19–22], as oxygen permeable membranes [23–25], as sensor material [26–28] or in catalyst systems [29–32]. The wide range of applications of perovskites means that CL-related research can build up on a wealth of detailed characterizations of the chemical and physical properties of these materials. We refer here to recent review papers giving a comprehensive overview of different compositions that have been investigated for the CL partial oxidation of CH_4 [33,34]; this work explores the $LaFeO_3$ family that has shown to possess oxygen storage capacities of ~ 10 wt% and to yield CH_4 conversions > 70 % at a CO selectivity > 90 % [35]. The actual formula of $LaFeO_3$ is $LaFeO_{3-}\delta$, where δ refers to the oxygen non-stoichiometry (or oxygen deficiency) that quantifies the amount of oxygen atoms incorporated into the crystal lattice of the perovskite.

Computational studies have shown that the energy of oxygen vacancy formation for $LaFeO_3$ perovskites is higher than that for $LaCoO_3$ or $LaMnO_3$ [36–41] and suggested that the lower oxygen mobility at high oxygen vacancy formation energies favours the partial oxidation of CH_4 rather than the total oxidation of CH_4 [42–44]. Early research on $LaFeO_3$ noted that the reducibility with CH_4 is relatively slow [45]. The oxygen mobility and the reactivity of $LaFeO_3$ increase upon substituting the A-site cation La^{3+} with Sr^{2+} [39,46–49]; to preserve charge neutrality, the oxidation state of the Fe in the B site increases accordingly from Fe^{3+} to Fe^{4+} or even Fe^{5+} [35,50,51]. Interestingly, bulk phase transitions of $LaFeO_3$ and related structures are often ignored [52], such that the significance of the computational simulations is limited to the perovskite host structure and the removal of non-stoichiometric lattice oxygen, i.e. that linked with a change of δ ($\Delta\delta = \delta - \delta_0$, where δ_0 is the value of the oxygen non-stoichiometry just before lattice oxygen is removed). Since δ varies with temperature and p_{O2}, the selectivity towards the reaction products may change depending on the initial value of δ_0. Many studies have assumed that the non-stoichiometry δ is zero in air at ambient temperature and pressure [53,54], which may be misleading when correlating selectivity with the amount of lattice oxygen removed. Perovskites tend to release non-stoichiometric lattice oxygen as gaseous O_2 when they are heated in an inert environment (e.g. Ar or N_2) while still maintaining structural stability until δ reaches its maximum value of 0.5 [55,56]. Further extraction of lattice oxygen requires a reducing gas, e.g. CH_4, and induces a phase transition. Thus, the amount of lattice oxygen removed that is proportional to Δδ can give an estimate of the initial non-stoichiometry of the oxygen carrier. It has been observed that in $LaFeO_3$ Δδ increases with substitution of the A-site cation La^{3+} with Sr^{2+} [57], which results in a higher amount of total oxidation products in the reaction with CH_4 owing to more reactive lattice oxygen linked with the increasing oxidation state of the Fe to maintain charge neutrality [39,58]. When perovskites are used for the CL-POx at high temperature (> 800 °C), different regions of selectivity have been observed: (i) The total oxidation of CH_4 due to "loose" lattice oxygen, (ii) the partial oxidation of CH_4, and (iii) the CH_4 decomposition resulting in the deposition of carbon on the surface of the oxygen carrier once it has been depleted in redox-active lattice oxygen [59–62]. Our previous work has shown that lattice oxygen that is unselective for the partial oxidation of CH_4 (and instead totally oxidizes CH_4) is associated with non-stoichiometric lattice oxygen within the perovskite structure [63]; however, lower absolute values of δ do not necessarily relate to a higher selectivity towards total oxidation products.

From the findings above we note there exists several aspects that have not been given much attention yet, in particular the role of bulk phase transitions associated with a constant p_{O2}. Lattice oxygen transfer associated with such phase transitions can enable a higher and stable selectivity towards partial oxidation products compared to when non-stoichiometric lattice oxygen (where the $p_{O2,eq}$ varies with δ) is used. Further, despite many studies emphasizing the potential of La-Fe-based and related perovskites for the chemical looping partial oxidation of CH_4, an extended demonstration without purge steps has not been performed yet. Here, we report on the rational development of an oxygen carrier with a relatively small degree of substitution of La^{3+} with Sr^{2+} (i.e. 15 %) that ensures that a large fraction of the total amount of redox-active lattice oxygen is selective for partial oxidation products in the reaction with CH_4. In the B site, 5 % of the Fe is substituted with Al to induce structural defects and to improve the reactivity of the oxygen carrier without compromising the total oxygen storage capacity appreciably [63]. The oxygen carrier with the nominal composition $La_{0.85}Sr_{0.15}Fe_{0.95}Al_{0.05}O_{3-}\delta$ is characterized in depth using inter alia thermogravimetry, fluidized and packed bed reactors, transient pulse experiments, XPS and in-situ XRD to relate structural changes to lattice oxygen transfer. We show that lattice oxygen can be 100 % selective towards the partial oxidation products provided bulk phase transitions are involved. Importantly, we demonstrate in an experiment over more than 45 days (equivalent to ~ 4050 redox cycles) that CH_4 (reductant) and CO_2 (oxidant) are completely converted into a synthesis gas – the longest continuously running experiment in CL to date. Lastly, we discuss potential process configurations for use of the oxygen carrier beyond POx.

2. Experimental

2.1. Material synthesis

The oxygen carrier used in this work was based on a lanthanum iron perovskite ($LaFeO_{3-}\delta$). Previous work suggested that the partially substitution of the A-site (La) with Sr and the B-site (Fe) with Al improves oxygen transfer under POx conditions [63]. Thus, an oxygen carrier with the nominal composition $La_{0.85}Sr_{0.15}Fe_{0.95}Al_{0.05}O_{3-}\delta$ was produced via granulation. Stoichiometric amounts of La_2O_3, SrO, Fe_2O_3 and Al_2O_3 were mixed and ball-milled to obtain a fine powder composed of particles < 1 µm; the mixture of metal oxides was provided by Euro Support Advanced Materials B.V.

Granulated particles were produced by vigorously stirring the fine powder with deionized water using pestle and mortar until aggregates formed. The aggregates were separated from the powder by sieving and eventually all powder was converted into particles within the sieve range 355–710 µm. The particles were calcined at 1300 °C for 12 h in air in a muffle furnace (heating rate of 5 °C min^{-1}). In the different experiments, three particle size fractions were used, < 50 µm, 180–212 µm and 355–500 µm.

2.2. Material characterization

The bulk density and porosity of the oxygen carrier were determined by measuring the weight and the tapped volume occupied by a given amount of particles in air.

The surface area and pore volume (based on the Brunauer-Emmett-Teller (BET) and Barrett-Joyner-Halenda (BJH) model, respectively) were determined using a NOVA 4000e analyzer (Quantachrome Instruments); samples were degassed under vacuum at 250 °C for 3 h prior to the actual N_2 adsorption and desorption measurements at 196 °C. No significant differences in surface area and pore volume were observed when measuring samples of the size < 50 µm or 355–500 µm.

The crushing strength of individual oxygen carrier particles (sieved to 355–425 µm) was obtained by measuring the force (normalized by the projected cross-sectional area of a particle) required to break them using a force gauge operated at 50 Hz (Shimpo, FGN-20); at least 50 measurements were performed to give meaningful results.

The actual elemental composition of the oxygen carrier was determined by inductively coupled plasma optical emission spectroscopy (ICP-OES) using an Agilent 5100 VDV instrument.

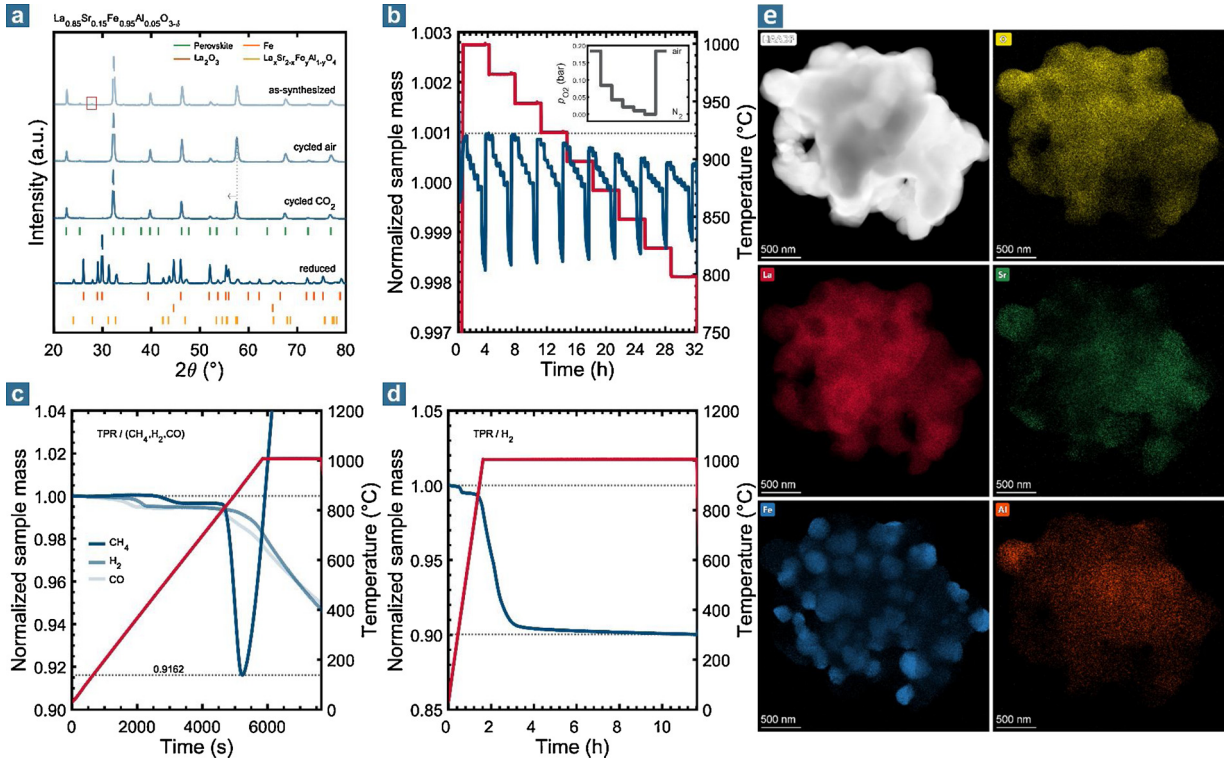

Fig. 1. (a) XRD patterns of as-synthesized, cycled (oxidized in air or CO_2) and reduced oxygen carrier. The red square indicates the position of a reflection due to an impurity phase. (b) Normalized sample mass of the oxygen carrier, as measured in the TGA as a function of temperature and p_{O2}. The inset illustrates the change of p_{O2} at each temperature. (c) Normalized sample mass of the oxygen carrier, as measured in the TGA in TPR experiments (10 °C min^{-1}) using 6.7 vol.% CH_4 or H_2 or CO in N_2. (d) Normalized sample mass of the oxygen carrier, as measured in the TGA in a TPR experiment (10 °C min^{-1}) using 6.7 vol.% H_2/N_2. The temperature was held at 1000 °C for 10 h. (e) HAADF image and corresponding EDX maps of the reduced oxygen carrier after the TPR shown in (d) (For interpretation of the references to colour in this figure legend, the reader is referred to the web version of this article).

Raman spectroscopy using a Thermo Scientific DXR Raman microscope (laser wavelength 455 nm) was employed to characterize carbon deposits on the surface of the reduced oxygen carrier.

A PANalytical Empyrean X-ray powder diffractometer (Cu Kα radiation, 45 kV and 40 mA) equipped with a X'Celerator Scientific ultrafast line detector and Bragg-Brentano HD incident beam optics was used to analyze the crystalline phases of the oxygen carrier. A monochromator was installed on the diffracted beam side to suppress fluorescence originating from the iron in the oxygen carrier. Each measurement lasted 3 h and was performed in the 2θ range of 20–80 ° with a step size of 0.016°. Refinement of the XRD patterns using the Rietveld method was performed using the software FullProf. An Anton Paar XRK 900 reactor chamber was used to study the evolution of crystalline phases upon oxidation of a reduced oxygen carrier sample (~ 20 mg) from 200 to 800 °C; note that it was not possible to investigate the reduction reaction in-situ since the reaction chamber itself was redox-active [64].

X-ray photoelectron spectroscopy (XPS) measurements were conducted on a Sigma II instrument (Thermo Fisher Scientific), which was equipped with an ultra-high vacuum chamber, a non-monochromatic 200 W Al Kα source, a hemispherical analyzer, and a seven-channel electron multiplier. Pass energies of 50 eV and 25 eV were set for the survey and the narrow scans, respectively. Exposure of the samples to ambient air was kept as short as possible (< 12 h) prior the measurements. The C 1s peak of adventitious carbon was set at 284.8 eV to compensate for any charge-induced shifts, recognizing that variations in binding energy can still occur [65].

Scanning transmission electron microscopy (STEM) images of ground oxygen carrier particles were obtained using a FEI Talos F200X microscope operated at 200 kV. The microscope was equipped with a high-brightness Schottky field-emission gun (FEG), a high-angle annular dark field (HAADF) detector and a large collection-angle energy-dispersive X-ray spectroscopy (EDX) detector. For measurements, samples were dispersed onto Cu grids and coated with lacey carbon. Scanning electron microscopy (SEM) of oxygen carrier particles was performed using a FEI Quanta 200 FEG microscope operated at 10 kV. The particles were sputter-coated with a thin layer of gold prior to imaging.

2.3. Reactivity characterization and performance evaluation in cyclic redox experiments

The reactivity of the oxygen carrier in cyclic redox experiments was investigated using (i) a thermogravimetric analyzer (TGA, Mettler Toledo DSC 1/3), (ii) a fluidized bed reactor (FBR), and (iii) a packed bed reactor (PBR). The gases used in these apparatuses were provided by Carbagas from cylinders (grade 5.0). The gas flow rates were measured and controlled at normal temperature and pressure (NTP) using mass flow controllers (Bronkhorst, EL-Flow). Blank experiments were performed for all experiments to account for e.g. buoyancy effects when switching gases (TGA), residual gas in manifolds (TGA/FBR/PBR), or gas-phase reactions (TGA/FBR/PBR). Details on the experiments performed in the TGA, FBR and PBR and the corresponding data analysis are given in the Supporting Information (SI).

3. Results and discussion

The first part of the results section deals with the physical and chemical characterization of the oxygen carrier when it transitions between its reduced and oxidized states. In the second part, the cyclic redox performance is assessed using a thermogravimetric analyzer (TGA), a fluidized bed reactor (FBR) and a packed bed reactor (PBR).

The third part presents the results from a cyclic experiment in the PBR lasting more than six weeks (equivalent to more than 4050 redox cycles). In the last part, possible process configurations are discussed in brief.

3.1. Part I – oxygen carrier characterization

3.1.1. Physical and chemical characterization

The oxygen carrier studied in this work had the nominal composition $La_{0.85}Sr_{0.15}Fe_{0.95}Al_{0.05}O_{3-}\delta$, which corresponded to a weight ratio of the metal elements (La:Sr:Fe:Al) of 0.636:0.071:0.286:0.007. The measured ratio (via ICP-OES, average of three samples) was 0.622(5):0.074(1):0.296(4):0.007(0) and was thus in good agreement with the nominal weight ratio, whereas the Fe content was slightly higher than intended. The as-synthesized oxygen carrier (i.e. after calcination in air for 12 h) was not a phase-pure perovskite, but contained an impurity phase (most likely $SrCO_3$) that induced a reflection at 27.8° in the diffractogram shown in Fig. 1a. Upon redox cycling (i.e. reducing the oxygen carrier and re-oxidizing it), the impurity phase disappeared and the oxygen carrier was phase-pure. The XRD pattern was fitted (Fig. S1 in SI) with an orthorhombic structure with the unit cell parameters a = 5.5492(5) Å, b = 7.8139(6) Å, and c = 5.5323(6) Å (space group *Pnma*). High-angle annular dark-field (HAADF) images and the corresponding EDX maps of La, Sr, Fe, Al and O confirm a homogeneous dispersion of all elements (Fig. S2 in SI). The disappearance of the impurity phase coincides with an "activation" period – an increase in reactivity – that has often been observed for oxygen carriers [55,63,66,67]; in this work, no further increase in reactivity was observed after typically the first 10–15 redox cycles at 900 °C. The specific surface area decreased slightly upon activation (from 1.3 to 0.8 $m^2 g^{-1}$, Table 1), suggesting activation for this oxygen carrier was related to structural rather than morphological changes. If not stated otherwise, only activated oxygen carrier was used in the experiments (i.e. oxygen carrier that had undergone at least 20 redox cycles at 900 °C). The particles produced had a bulk density of ~ 1760 kg m^{-3}, which was lower than that reported for $La_{0.85}Sr_{0.15}FeO_{3-\delta}$ (~ 2430 kg m^{-3}) in our previous study [63]. Assuming a void fraction of 45 % when measuring the bulk density, the particle density was ~ 3200 kg m^{-3}. Taking the unit cell volume from the refined XRD pattern (239.9 $Å^3$), the true material density was estimated to be 6280 kg m^{-3}, and so the particle porosity was ~ 49 %.

The oxygen non-stoichiometry δ takes values between 0 and 0.5 for most perovskites [56]. La-Fe-based perovskites with a low degree of substitution of La with Sr typically possess low values of δ with oxidation states of the Fe slightly greater than 3+ [35,39]. The value of δ depends on the combination of temperature and partial pressure of oxygen (p_{O2}); typically, δ increases with increasing temperature for a given p_{O2} [68]. Note that reliable, direct measurements of δ via titration could, unfortunately, not be made in this work. Fig. 1b shows how the normalized weight of the oxygen carrier changed with temperature (between 800 and 1000 °C) and p_{O2} (between ~ 0 and 0.18 bar). The sample weight equilibrated readily with the p_{O2} of the gas environment through the adjustment of the structural parameter δ and the release or uptake of gaseous O_2. Different from what is usually observed, the normalized sample weight decreased slightly with decreasing temperature for a given p_{O2}, indicating that δ was lowest at the maximum temperature investigated (i.e. 1000 °C).

3.1.2. Temperature-programmed reduction / oxidation

The oxygen storage capacity, i.e. the weight fraction of redox-active lattice oxygen, was determined via thermogravimetry by heating the oxygen carrier from 25 °C to 1000 °C in 6.7 vol.% of a reducing gas (CH_4, H_2 or CO). From Figs. 1c and S3 – S5 in SI it is evident that the reducibility of the oxygen carrier was much higher in CH_4 than in H_2 or CO for a given time. The weight loss occurred in two principle steps; the first decrease in normalized sample weight (from 1 to ~ 0.995) linked with the production of total oxidation products [39] was observed in the range of 440–590 °C for CH_4, ~ 325–400 °C for H_2 and ~ 275–375 °C for CO, whereas the second, much greater decrease started at ~ 800 °C. The lower apparent reactivity of the oxygen carrier with H_2 and CO at high temperature was not the result of poor kinetics, but related to the thermodynamic properties of the oxygen carrier in conjunction with the quality of mass transport in this particular type of TGA: As has been shown for similar material compositions [35] (and is shown for this oxygen carrier in 3.2.2), the equilibrium ratio of H_2/H_2O or CO/CO_2 is greater than ~ 20 when reducing the oxygen carrier, which means that only a small fraction of H_2 or CO can thermodynamically be converted into H_2O or CO_2. The presence of H_2O or CO_2 in the vicinity of the surface of the oxygen carrier (i.e. the gas-solid interface where the reactions H_2 + [O] → H_2O or CO + [O] → CO_2 take place) inhibits the conversion of H_2 and CO further. Mass transport in the TGA used in this work is dominated by vertical counter-diffusion of gas to/from the sample inside the crucible [69,70], implying that the removal of product gas (i.e. H_2O or CO_2) from the gas-solid interface is slow and so explains the low observed rate of reduction for H_2 and CO in Fig. 1c.

When CH_4 was used as the reductant, the minimum normalized sample weight of 0.916 was observed before the temperature reached the maximum temperature of 1000 °C (Fig. 1c). The actual oxygen storage capacity was higher than (1 – 0.916 =) 8.4 wt%, because the measured weight curve reflects overlapping effects of weight decrease due to the loss of lattice oxygen, and weight increase due to the accumulation of carbon on the surface of the oxygen carrier ($CH_4 \rightarrow 2\ H_2$ + C). The thermal decomposition of CH_4 is favored at high temperature, is catalyzed by metallic iron [71] and became significant in our work when the oxygen carrier lost more than ~ 7 % of its initial weight due to the transfer of its lattice oxygen to the reducing gas; this is discussed in detail in 3.2.1. Reliable measurements of the oxygen storage capacity hence require the reduction of the oxygen carrier to be performed in the absence of side reactions that would impair the recorded weight changes. Fig. 1d plots the normalized sample weight measured under 6.7 vol.% H_2/N_2 for an extended time to allow for the near-complete reduction of the oxygen carrier; the oxygen storage capacity was 9.6 ± 0.2 wt% (average of five measurements). As mentioned above, the value of δ increased slightly from 1000 to 900 °C, and so the effective oxygen storage capacity at 900 °C (i.e. the reaction temperature most frequently used in this work) was minimally lower. In this work, the effective oxygen storage capacity was estimated conservatively to be 9 wt%, equivalent to 2.8 mmol of O_2 per g oxygen carrier.

Rietveld refinement of the X-ray diffraction (XRD) pattern of the reduced oxygen carrier (Fig. 1a) suggests that the reduced oxygen carrier consisted of 47.8 wt% La_2O_3, 29.2 wt% $La_xSr_{2-x}Fe_yAl_{1-y}O_4$ (which possessed a tetragonal K_2NiF_4 structure [72]), and 23 wt% Fe (Fig. S6 and Table S1 in SI). EDX maps showing the distribution of the elements within the reduced oxygen carrier in Fig. 1e imply that most

Table 1
BET surface area and BJH pore volume of oxygen carrier particles (355–500 µm).

State of the oxygen carrier (oxidized in air)	BET surface area ($m^2 g^{-1}$)	BJH pore volume (µl g^{-1})
As-synthesized (calcined at 1300 °C)	1.3	2
Activated (after 20 redox cycles at 900 °C)	0.8	2
Cycled (after > 100 h of redox cycling)	0.8	2

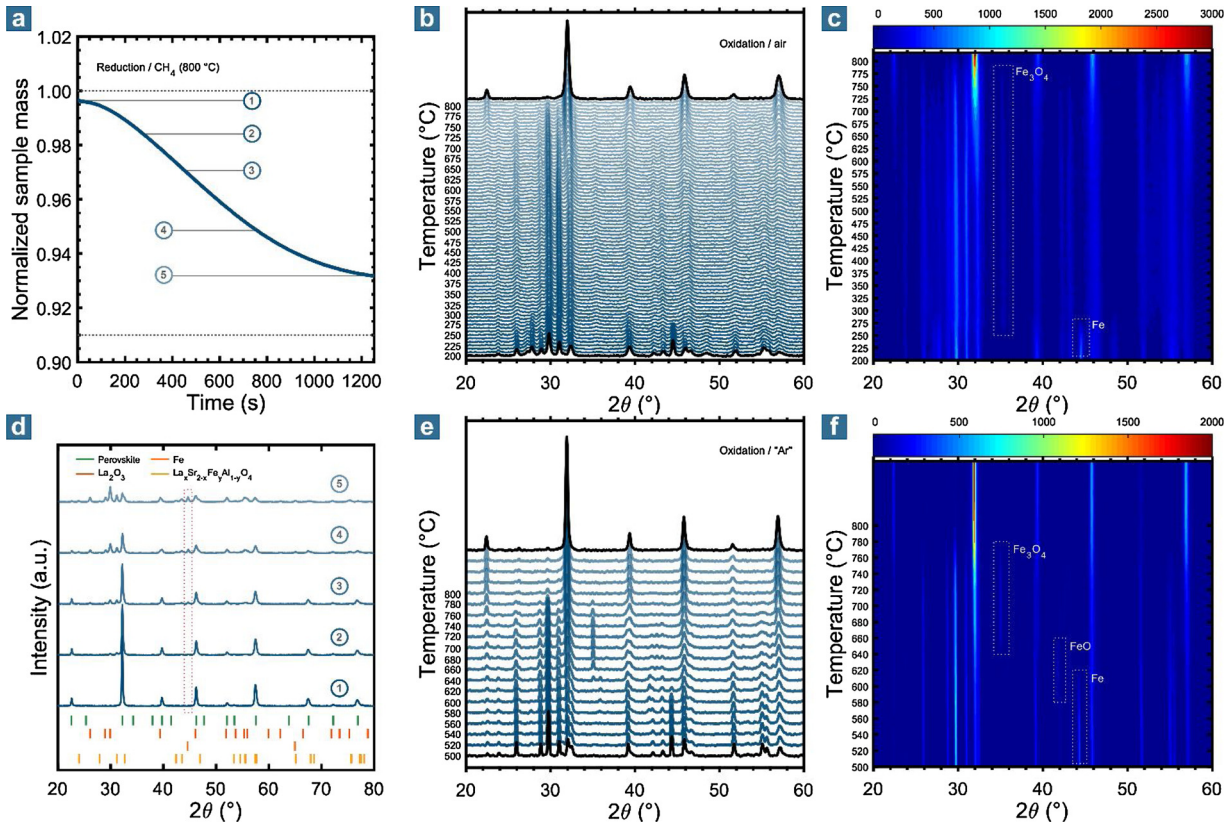

Fig. 2. (a) Normalized sample mass of the oxygen carrier shown as a function of time, as measured in the TGA during reduction at 800 °C using 6.7 vol.% CH_4 in N_2. Samples were collected at different degrees of reduction (1–5) with the corresponding XRD patterns shown in (d); the grey horizontal dashed lines indicate the maximum and minimum normalized sample mass for full oxygen carrier conversion. (b) In-situ XRD patterns collected between 200 and 800 °C when a reduced oxygen carrier was re- oxidized in air. (c) 2D contour plot of the XRD patterns shown in (b). (d) XRD patterns of oxygen carrier for different extents of reduction shown in (a). The red dashed rectangle indicates the evolution of the main diffraction peak at 44.6° due to metallic Fe. (e) In-situ XRD patterns collected between 500 and 800 °C when a reduced oxygen carrier was re-oxidized in "Ar". (f) 2D contour plot of the XRD patterns shown in (e) (For interpretation of the references to colour in this figure legend, the reader is referred to the web version of this article).

of the Fe was separated from the other crystalline phases in aggregates of up ~ 400 nm, and that Al existed only within the $La_xSr_{2-x}Fe_yAl_{1-y}O_4$ phase. From a mass balance using the results from the ICP-OES measurements, the values of x and y were ~ 1.1 and ~ 0.7, respectively. A mixture of different phases was visible when the oxygen carrier was reduced only partially (Fig. 2a,d), which implied that the oxygen carrier underwent a bulk phase transition beginning when very little lattice oxygen was removed.

In a temperature-programmed oxidation (TPO) experiment using air, most of the lattice oxygen was replenished between 375 and 450 °C in a strongly exothermic reaction (Fig. S7 in SI). Interestingly, upon heating the oxygen carrier further, the normalized sample weight was lower in the range 700–900 °C compared to < 700 °C and > 900 °C, indicating that multiple phase transitions occurred that are linked with different oxidation states. Oxidation of the reduced oxygen carrier was also feasible with CO_2 and even N_2 (Figs. S8 and S9 in SI); note that the N_2 used (grade 5.0) contained ~ 10 ppm of O_2. Using CO_2 as the oxidant, again multiple phase transitions were identified from the curve of the normalized sample weight (Fig. S8 in SI). In the TPO with N_2 (Fig. S9 in SI), most of the redox-active lattice oxygen was recovered. The normalized sample weight increased slightly when adding air to the N_2 flow (inset in Fig. S9), in agreement with the results shown in Fig. 1b. The difference in the oxidation potentials of air, CO_2 and "N_2" is reflected by the different oxidation states of the oxygen carrier at the end of the oxidation reaction, which in turn cause structural variations. Fig. 1a shows that the positions of the characteristic peaks in the XRD pattern were shifted towards lower diffraction angles when the oxygen carrier was re-oxidized in CO_2 instead of air; the corresponding perovskite unit cell parameters were a = 5.5573(4) Å, b = 7.8624(6) Å, and c = 5.5333(4) Å (Fig. S10 in SI), translating into an increase in unit cell volume over the sample oxidized in air [73]. Note that the normalized sample weights measured at the end of the TPOs for the different oxidants (Figs. S7 – S9 in SI) did not reflect the differences in oxidation states of the oxygen carrier – the normalized sample weight of the sample oxidized in air should be higher than that of the sample oxidized in CO_2 – which was probably owing to different initial sample weights (i.e. slightly different degrees of reduction). Importantly, upon exposure to CH_4 a further shift towards lower diffraction angles was not seen in the XRD pattern in Fig. 2d, although there was still a relatively high amount of non-stoichiometric oxygen within the perovskite structure present given the low amount of lattice oxygen removed (e.g. points 2 and 3 in Fig. 2a). Therefore, oxygen removal from the oxygen carrier was largely linked with a bulk phase transition, rather than an increase in δ until the maximum value of δ = 0.5 is reached for a structurally stable perovskite.

3.1.3. *In-situ X-ray diffraction*

The high affinity of the reduced oxygen carrier for oxidants was apparent from the change of its color upon long exposure to ambient air. The reduced oxygen carrier was black, oxygen carrier oxidized in CO_2 was yellow/ocherous/red (the color varied within a very narrow range of conversion), and the oxygen carrier oxidized in air was dark grey. The color of the red oxygen carrier powder (oxidized in CO_2) changed consecutively to dark red, brown and grey when stored in a drying oven at 80 °C for two weeks. In-situ XRD was performed to understand the transition between phases upon reduction/oxidation. The

sample was heated from 25 to 800 °C at a rate of 10 °C min^{-1} under a flow of 200 ml min^{-1} of air. Every 25 °C, the temperature was held for 30 min during which three measurements in the 2θ range of 20–60 ° were made; the diffractograms are plotted in Fig. 2b and are presented in Fig. 2c as a D contour plot. Starting from ~ 275 °C, the metallic Fe phase (main diffraction peak at 44.6°) transformed to Fe_3O_4 (main diffraction peak at 35°). The final perovskite structure began to form only at ~ 700 °C, when also the reflections due to Fe_3O_4 gradually vanished. These observations are consistent with the TPO in air (Fig. S7 in SI), where a significant structural transformation was observed near 700 °C. The weight curve measured in the TPO with CO_2 that has a much lower oxidation potential than air suggests at least one additional phase transition (Fig. S8 in SI), which was investigated by performing the in-situ XRD experiment in Ar. Owing to O_2 impurities, Ar (grade 5.0) possessed a p_{O2} that was much smaller than that of air and more suited to observe intermediate phases given the relatively low time resolution of the XRD instrument. The results plotted in Fig. 2e and f show that the metallic Fe phase was first transformed to FeO (main diffraction peak at 42°) at ~ 580 °C, and then to Fe_3O_4 at ~ 640 °C. The final perovskite structure formed at ~ 780 °C when the Fe_3O_4 phase disappeared. Similar to the experiment in which air was used as the oxidant, only additional phase transitions related to the initial metallic Fe were observed (i.e. Fe → FeO → Fe_3O_4), and the La_2O_3, $La_xSr_{2-x}Fe_yAl_{1-y}O_4$ and Fe_3O_4 phases transformed to the perovskite phase in a single step. At 800 °C, air was added to the Ar flow, resulting in a shift of the characteristic peaks in the XRD pattern towards larger diffraction angles (Fig. S11 in SI) due to the additional oxygen incorporated in the structure (equivalent to a decrease in the value of δ, see also Fig. 1a).

Lastly, in a third in-situ XRD experiment, the reduced oxygen carrier was heated in 5 vol.% CH_4/N_2 to 800 °C to avoid early oxidation. At 800 °C, the flow of CH_4 was stopped and only N_2 was flown over the sample for 5 min. After one measurement (10 min), the oxygen carrier was fully oxidized and only reflections due to the perovskite phase were observed. Performing the same experiment at 600 °C resulted in the formation of an Fe_3O_4 phase, but no further oxidation to form the perovskite phase occurred (the experiment was terminated after 7 h). The in-situ XRD experiments revealed that the formation of the FeO/Fe_3O_4 phases at low temperature (< 600 °C) inhibited the direct transition of the La_2O_3, $La_xSr_{2-x}Fe_yAl_{1-y}O_4$ and Fe phases to the perovskite phase. At high temperature (> 800 °C), the direct formation of the perovskite phase was favored over the formation of Fe_3O_4 even in very low p_{O2} environments.

3.1.4. Pulse experiments

The formation of gaseous reaction products has not been considered yet in Section 3.1. Previous studies using similar perovskite-based oxygen carriers for the POx reaction have reported that the oxygen carrier undergoes several stages upon reduction, with varying selectivity towards total and partial oxidation products of CH_4 that imply mechanistic differences in the transfer of lattice oxygen to the CH_4 [59–62]. Pulse experiments are a useful tool to assess the selectivity towards products as a function of conversion of the oxygen carrier [74,75]. Here, the fully oxidized oxygen carrier (180–212 µm) was exposed to 200 pulses of CH_4 through a 0.1 ml sample loop at ~ 910 °C; Ar (grade 5.0) was used as the carrier gas. Assuming an average CH_4 conversion of 50 %, ~ 240 pulses were theoretically needed to reduce the oxygen carrier completely. The results of two of such experiments are shown in Fig. 3a and b, with the only difference being the time between consecutive pulses (170 vs. 110 s). The signals for each m/z were normalized to the respective maximum intensity observed over the 200 pulses, and they are presented on a linear scale.

In the experiment with a time lag of 170 s between consecutive pulses (Fig. 3a), CH_4 was rapidly converted into the total oxidation products CO_2 and H_2O at the very beginning. The signal intensity of CO_2 and H_2O decreased with the number of pulses and eventually became insignificant after ~ 10 pulses of CH_4 injected. The reverse trend was observed for the partial oxidation products CO and H_2, which were the dominant gaseous species produced after ~ 10 pulses. The conversion of CH_4 was highest in the very first pulse when CH_4 was totally oxidized to CO_2 and H_2O, as can be seen from the relatively low intensity of the m/z 15 signal (the m/z 15 signal was preferred over the m/z 16 signal to avoid cross-sensitivities with CO, CO_2, H_2O and O_2). When the partial oxidation was dominant (after ~ 10 pulses), the CH_4 conversion increased slightly with the number of CH_4 pulses (and thus the extent of reduction of the oxygen carrier). No thermal decomposition of CH_4 was observed, as the intensities of the signals corresponding to CO and H_2 followed the same, continuously increasing trend.

The principal trend in the mass spectrometer signals was similar in Fig. 3b when the time between consecutive pulses of CH_4 was reduced from 170 to 110 s. However, the total oxidation products vanished after a smaller number of pulses and partial oxidation products became dominant after only 3–4 pulses of CH_4. After ~ 120 pulses, the intensity of the m/z 28 (CO) signal decreased, whereas the intensity of the m/z 2 (H_2) signal increased, implying (i) that the oxygen carrier became close to being depleted in redox-active lattice oxygen, and (ii) that the thermal decomposition of CH_4 became significant. The conversion of CH_4 appeared slightly higher when CH_4 decomposed thermally (> 120 pulses) compared to when CH_4 was partially oxidized (< 120 pulses).

Previous works have reported on a “relaxation” effect related to the transfer of lattice oxygen from the bulk of the oxygen carrier to its surface [76,77]: When the time between consecutive pulse injections was increased, a decreasing selectivity towards synthesis gas was observed and total oxidation products appeared again. The results of our measurements shown in Fig. 3a and b point in a similar direction and at the beginning of the experiment (first ~ 5 pulses), a longer time between consecutive pulses resulted in a lower selectivity towards CO and H_2. Yet, the underlying reason was not a “relaxation” effect (that would depend also on the physical properties of the oxygen carrier), but simply the result of the re-oxidation of the oxygen carrier with traces of O_2 contained in the Ar carrier gas, which happened between consecutive pulses of CH_4. Our TPO (Fig. S9 in SI) and in-situ XRD measurements (Fig. 2e,f) showed that the oxygen carrier can readily be oxidized in extremely low p_{O2} environments. The complete reduction of the oxygen carrier was not achieved in our pulse experiments within a reasonable time when the time between consecutive pulses was greater than 1 min. We also note that the switching valves accommodating the sample loop must be contained in an inert environment, as otherwise additional O_2 from ambient air will diffuse into the valve and contribute to the re-oxidation of the oxygen carrier. The oxygen carrier, once reduced to some degree, is extremely efficient in removing oxidants from a gas stream at high temperature. We observed that the re-oxidation was feasible using N_2, Ar or He (all grade 5.0) and no oxidants (O_2, CO_2 or H_2O) were detected by mass spectrometry until breakthrough (i.e. when the oxygen carrier was fully oxidized) despite detection limits in the ppb range. Thus, what has been referred to as a “relaxation” effect in other works may have been the result of oxidizing impurities in the carrier gas too. The overlapping effects of reduction and oxidation during the pulse experiments make an accurate determination of the conversion of the oxygen carrier extremely difficult.

Different stages of selectivity towards synthesis gas were observed in the pulse experiments, which have been related to selective and unselective oxygen species on the surface of the oxygen carrier [59,76,78]. X-ray photoelectron spectroscopy (XPS) was employed to distinguish between different types of oxygen species and the oxidations states of the metal elements for different degrees of oxygen carrier conversion, i.e. oxidized in air, oxidized in CO_2 and reduced (after the TPR shown in Fig. 1d). Fig. 3c shows the corresponding O 1s XPS spectra, which were deconvoluted into two peaks that were sufficient for an excellent agreement with the measured data. The two peaks reflect lattice oxygen (O_I, binding energy ~ 529.8 eV) and chemically adsorbed oxygen (O_{II}, binding energy ~ 532 eV); physically adsorbed oxygen species have been reported for higher binding energies [39] but

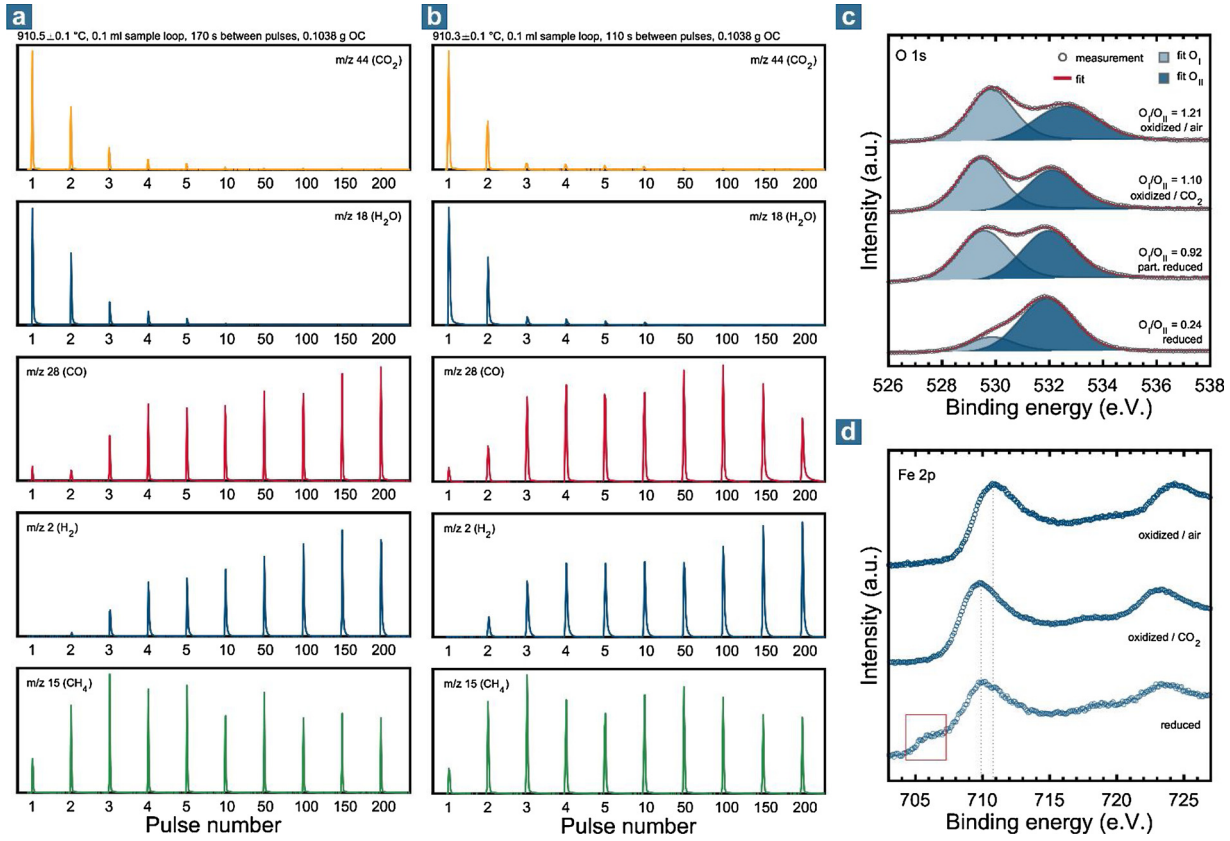

Fig. 3. (a) Measured signals of various *m/z* in response to pulses of CH_4 over the oxygen carrier; the time between consecutive pulses was 170 s and 200 pulses were injected. (b) Measured signals of various *m/z* in response to pulses of CH_4 over the oxygen carrier; the time between consecutive pulses was 110 s and 200 pulses were injected. (c) XPS spectra in the O 1s region measured for oxidized (air / CO_2) and reduced (partially / completely) oxygen carrier; measurements were deconvoluted into two peaks. The partially reduced oxygen carrier was reduced in CH_4 for 1 min in the TGA at 900 °C. (d) XPS spectra in the Fe 2p region measured for oxidized (air / CO_2) and reduced oxygen carrier. The vertical grey dotted lines indicate a shift in peak position. The red square indicates the position of a feature due to metallic Fe (For interpretation of the references to colour in this figure legend, the reader is referred to the web version of this article).

were not observed in our measurements such that a third or fourth deconvolution peak would have improved the quality of the fit significantly. O_I has been linked with nucleophilic oxygen (O^{2-} in the lattice) that is selective for partial oxidation products, whereas O_{II} has been linked with electrophilic oxygen species that lead to the formation of total oxidation products [78,79]. The ratio of the areas under the two peaks, O_I/O_{II}, decreased with conversion, consistent with O_I being the dominant redox-active oxygen species [80,81]. The ratio O_I/O_{II} = 1.21 measured for the fully oxidized oxygen carrier is within the range that has been observed by others for similar material compositions [44,82]. However, unique features from the O 1s XPS spectra that could be related to selectivity for the total or partial oxidation of CH_4 were not identified, and the ratio O_I/O_{II} appeared to change proportionally with conversion.

Fig. 3d shows the Fe 2p XPS spectra which feature two main peaks, Fe $2p_{3/2}$ at low binding energies and Fe $2p_{1/2}$ at higher binding energies. A shift in peak position is apparent when comparing the samples oxidized in air and CO_2, which implies a decrease in the oxidation state of the Fe [83]; determining the exact oxidation states requires XPS measurements at higher resolution to analyze better the position of satellite peaks, or ^{57}Fe Mössbauer spectroscopy [35,84]. The satellite peaks observed near ~ 717 eV in the spectra of the sample oxidized with CO_2 and the reduced sample are indicative of Fe^{3+}. In the reduced sample, the shoulder at ~ 706 eV is characteristic of metallic Fe [83], as expected from the XRD measurements in Fig. 1a. Therefore, the Fe 2p XPS spectra show that Fe existed in at least two different oxidation states in the reduced sample corresponding to the metallic Fe and $La_xSr_{2-x}Fe_yAl_{1-y}O_4$ phases. From a mass balance based on the Rietveld refinement shown in Fig. S6 in SI, > 85 % of the Fe contained in the parent perovskite was reduced to metallic Fe; the effective oxygen storage capacity of ~ 9 wt% was thus a result of the change in oxidation state of the Fe from Fe^{3+}/Fe^{4+} to Fe°.

The La 3d XPS spectra plotted in Fig. S12 in SI contained two spin-orbit components (La $3d_{5/2}$ at low binding energies and La $3d_{3/2}$ at higher binding energies), which were further split by multiplet splitting upon reduction. The magnitude of the splitting (i.e. the difference in binding energy between the pairs of peaks) can relatively reliably be related to different lanthanum compounds [85]. XRD in Figs. 1a and S6 in SI showed that La_2O_3 was the dominant crystalline phase in the reduced oxygen carrier, so that the difference in binding energy was expected to be ~ 4.6 eV [83]. The actual difference was only ~ 3.7 eV (Fig. S12 in SI), suggesting that hydroxy and, or, carbonate phases were present on the surface of La_2O_3 [85,86]. The Sr 3d and Al 2 s XPS spectra are shown in Figs. S13 and S14 in SI for completeness.

3.2. Part 2 – Assessment of the cyclic performance in different reactors

3.2.1. Thermogravimetric analyzer (TGA)

In this study, off-gas from the TGA was analyzed simultaneously by infrared and thermal conductivity sensors to relate conversion of the oxygen carrier with the type of products formed. The oxygen carrier was first reduced in 6.7 vol.% CH_4/N_2 and then sequentially oxidized in 6.7 vol.% CO_2/N_2 and 83.3 vol.% air/N_2; each reaction step lasted 9 min. Purge steps with pure N_2 (grade 5.0) of 1 min each were performed between the reducing and oxidizing reaction steps for data analysis purposes. At least 20 redox cycles were performed using

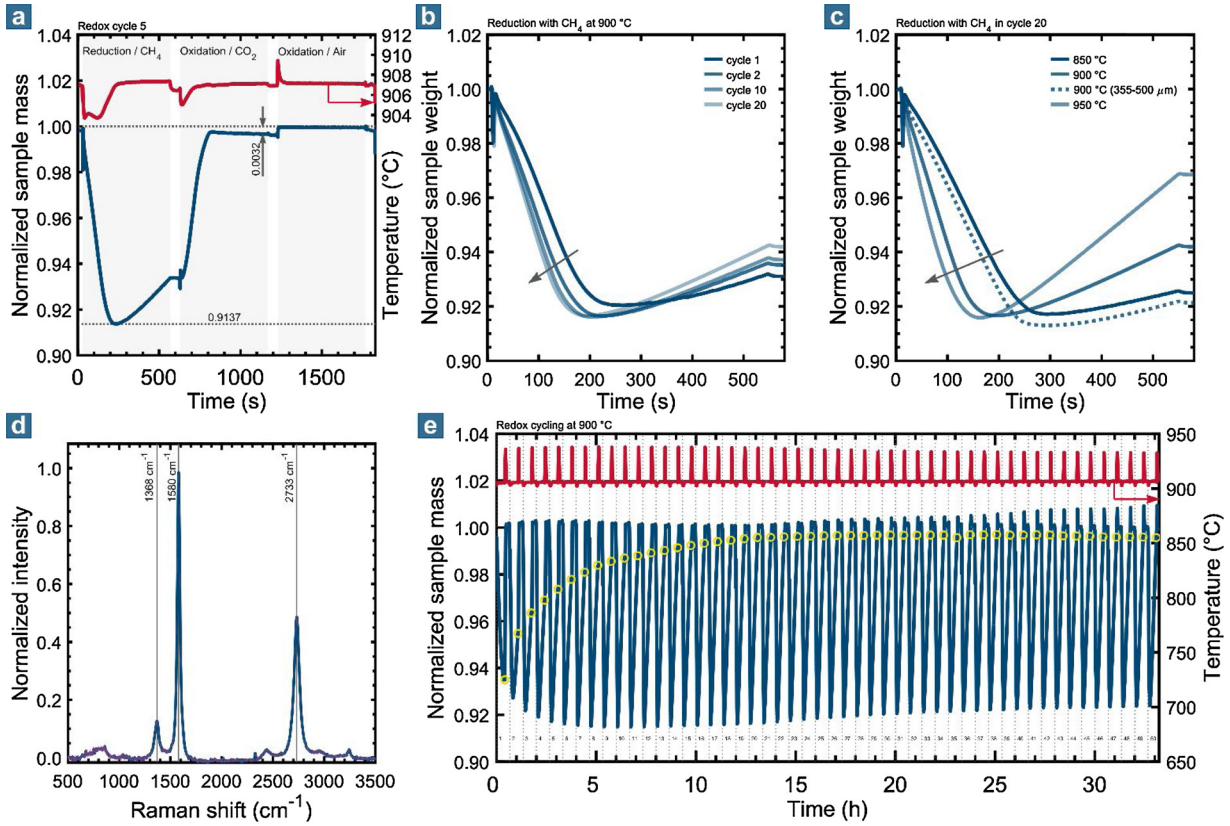

Fig. 4. (a) Normalized sample mass and temperature of the oxygen carrier measured in the TGA, shown as a function of time during the fifth of 20 redox cycles. (b) Normalized sample mass of the oxygen carrier measured during the reduction step in the TGA, shown for various cycle numbers. The grey arrow indicates increasing cycle number. (c) Normalized sample mass of the oxygen carrier measured during the reduction step in the TGA, shown for various temperatures. The grey arrow indicates increasing temperature. (d) Raman spectra measured for the oxygen carrier after the TPR in CH_4. The vertical grey lines indicate the position of the D, G and 2D bands, respectively, characteristic for carbon species. The pattern shown was averaged from spectra measured for six different areas; the red error bounds representing two standard deviations illustrate the good repeatability of the measurements. (e) Normalized sample mass and temperature of the as-synthesized oxygen carrier (355–500 μm) measured in the TGA over 50 redox cycles (Reduction in 6.7 vol.% CH_4/N_2, oxidation in 83.3 vol.% air/N_2). The yellow circles indicate the normalized sample weight measured at the end of each reduction step (For interpretation of the references to colour in this figure legend, the reader is referred to the web version of this article).

activated oxygen carrier (< 50 μm) at 850, 900 and 950 °C.

Fig. 4a shows exemplarily the normalized sample weight and temperature recorded during a complete redox cycle. Similar to what was observed in the TPR experiments, reduction with CH_4 was fast, occurred in one reaction step and the minimum sample weight (corresponding roughly to the time when the oxygen carrier was depleted in redox-active lattice oxygen) was reached after less than 5 min. The increase in normalized sample weight during the reduction step was due to the weight of carbon deposited on the oxygen carrier surface from the thermal decomposition of CH_4 ($CH_4 \rightarrow 2\ H_2 + C$). From the change in measured sample temperature it is clear that the reduction reaction was endothermic. The decomposition of CH_4 catalyzed by the metallic Fe phase of the oxygen carrier is also endothermic (~ 90 kJ mol^{-1} at 900 °C), but did not affect the sample temperature (and the measured heatflow) significantly. Owing to the overlapping effects of weight decrease due to the reduction reaction and weight increase due to carbon deposition, the actual onset of carbon deposition was determined from the measured mole fractions of H_2 and CO, shown in Fig. S15 in SI, and related to the normalized sample mass. At reaction temperatures of 850, 900 and 950 °C, the ratio of H_2/CO increased to values > 2 (i.e. the theoretical ratio for the POx reaction) when the normalized sample mass reached a value of ~ 0.93, and so indicated that the decomposition of CH_4 occurred as a side reaction. Note that the TGA and the gas analysis were synchronized to account for the response of the gas analyzers and the time needed for the gas to travel from the TGA reaction chamber to the gas analyzer. The reducibility of the oxygen carrier was relatively stable with cycling (Fig. 4b) and increased with temperature (Fig. 4c). When using large (355–500 μm) instead of small particles (< 50 μm), the reducibility decreased slightly owing to the greater intraparticle diffusion resistance (Fig. 4c). From the heatflow measured during the reduction step, the heat of reaction was estimated as ~ 425 kJ per mol of O_2at 900 °C, assuming an oxygen storage capacity of 9 wt% (note that the amount of lattice oxygen reacted has been converted to moles of O_2 to ease comparison with gas-phase reactions). This estimate is equivalent to 212.5 kJ per mol of CH_4, and is thus slightly lower than the heats of reaction for the steam reforming of CH_4 ($CH_4 + H_2O \rightarrow 3\ H_2 + CO$, 226 kJ mol^{-1}) and the dry reforming of CH_4 ($CH_4 + CO_2 \rightarrow 2\ H_2 + 2\ CO$, 259 kJ mol^{-1}). The sum of the heats of the reduction reaction of the oxygen carrier with CH_4 and the oxidation reaction with air is the same as that of the POx reaction ($CH_4 + 0.5\ O_2 \rightarrow 2\ H_2 + CO$, −23 kJ mol^{-1}), and so the heat of the oxidation with air is estimated to be −471 kJ per mol of O_2.

Carbon deposited on the surface of the reduced oxygen carrier during the TPR with CH_4 was characterized by Raman spectroscopy (Fig. 4d). The three main peaks observed at 1368, 1580 and 2733 cm^{-1} correspond to the D, G and 2D bands, respectively; the ratio of the intensities of these bands varies depending on the structure of the carbon [87,88]. The ratio of the intensities of the D peak to the G peak (I_D/I_G) was ~ 0.14, characteristic for polycrystalline graphite of relatively high structural order [88]. Such type of carbon is typically more resistant to oxidation and gasification than less ordered carbon with a higher number of defects and a high I_D/I_G [89,90]. We note that the final

temperature of the TPR (1000 °C) was higher than the reaction temperatures used in the experiments in the TGA, FBR and PBR, which may have affected the properties of the carbon. The Raman analysis of samples with carbon deposits from experiments performed at 900 °C gave an average $I_D/I_G \approx 0.29$, which was slightly lower, but still indicative of polycrystalline graphite.

Turning to the oxidation reactions in Fig. 4a, it can be seen that the carbon removal and the re-oxidation with CO_2 occurred quickly. The normalized sample weight at the end of the oxidation step with CO_2 was ~ 0.997, suggesting that ~ 3–3.5 % of the total redox-active lattice oxygen (for an oxygen storage capacity of 9 wt%) contributed to the total oxidation of CH_4 that was observed in the pulse experiments. As will be seen more clearly in the experiments using the FBR in 3.2.2, the oxidation reaction with CO_2 was mildly exothermic, whereas the carbon gasification reaction with CO_2 ($C + CO_2 \rightarrow 2\,CO$, 169 kJ mol^{-1}) or H_2O ($C + H_2O \rightarrow H_2 + CO$, 136 kJ mol^{-1}) is endothermic, resulting in a net temperature decrease in Fig. 4a. The oxidation reaction with air recovered the initial sample weight completely in an exothermic reaction. For completeness, the results of the cycling experiments performed at 850, 900 and 950 °C, including the measured off-gas concentration profiles, are summarized in Figs. S16 – S18 in SI and show a stable performance of the oxygen carrier.

The long-term stability and sinter-resistance of the as-synthesized oxygen carrier (355–500 µm) was assessed in a 50-cycle experiment at 900 °C using only air (83.3 vol.% air/N_2) in the oxidation step; the temperature increase was thus much higher compared to when an additional oxidation step with CO_2 was included (Fig. 4e). The period of activation lasted ~ 20 redox, as can be seen from the normalized sample weight at the end of the reduction step (indicated through yellow circles). Therefore, the time required for the complete reduction of the oxygen carrier decreased with cycle number, and the extent of carbon deposition increased accordingly.

We note that performance parameters, such as the conversion of CH_4, were not calculated from the measurements of the TGA experiments, because the TGA is in itself not suitable for such measurements owing to poor gas-solid contact efficiencies. Consequently, FBR and PBR experiments were performed with two distinct gas-solid contact patterns that enable (i) the uniform conversion of the entirety of the oxygen carrier particles in the FBR, and (ii) the gradual, local conversion of the oxygen carrier particles in the PFR through reaction fronts.

3.2.2. Fluidized bed reactor (FBR)

Experiments in the FBR were performed in a similar fashion as in the TGA and PBR, viz. in three steps at the set reactor temperatures ranging from 800 to 950 °C: Reduction was performed in 8.6 vol.% CH_4/N_2, followed by re-oxidization of the oxygen carrier first in 7.1 vol.% CO_2 or H_2O/N_2 and then in 85.7 vol.% air. Purge steps with pure N_2 (grade 5.0) for 3 min each were performed between the reducing and oxidizing reaction steps for data analysis purposes The bed consisted of oxygen carrier particles (355–500 µm) only to observe better phenomena such as the sintering or the agglomeration of the particles, which may remain unobserved when inert bed material is added.

Similar to our previous observations [63], the bed temperature decreased by > 30 °C during the endothermic reduction reaction and the total amount of synthesis gas produced increased with time of reduction and conversion of the oxygen carrier (Fig. 5a). CO_2 (and H_2O) was produced only at the very beginning of the reduction reaction, consuming ~ 3.4 % of the oxygen carrier's total redox-active lattice oxygen in the experiment performed at 900 °C. Note that the mole fraction of H_2O was not measured in these experiments and it was assumed that the total oxidation of CH_4 occurred according to $CH_4 + 4\,[O] \rightarrow 2\,H_2O + CO_2$ in the calculations of lattice oxygen consumption. At 800 °C, ~ 3.7 % of the oxygen carrier's total redox-active lattice oxygen was consumed for the total oxidation of CH_4, and at 950 °C the value decreased to ~ 3.1 %. The values are in good agreement with the TGA measurements in Fig. 4a and the trend with temperature is consistent with the results shown in Fig. 1b: The fully-oxidized oxygen carrier released gaseous O_2 under the N_2 environment just before the reduction step and the amount of oxygen released increased slightly with temperature (Fig. 1b), leaving effectively less lattice oxygen that was selective for the total oxidation of CH_4. After the initial peak of CO_2, > 99 vol.% of the off-gas consisted of H_2, CO and unconverted CH_4, with traces of CO_2 (but no H_2O) present.

The conversion of CH_4 increased with conversion of the oxygen carrier (i.e. the removal of lattice oxygen and increasing number of oxygen vacancies [91–94]), and so to ease a comparison for different temperatures, the conversion of CH_4 is reported in Fig. 5b for an oxygen carrier conversion of 20 %; this also allows for a comparison with the results from the PBR in 3.2.3. The conversions of CH_4 in Fig. 5b are thus much lower than the maximum conversions observed. For example, at a set temperature of 925 °C the conversion of CH_4 was > 92 % for oxygen carrier conversions > 40 %, but was only 85 % for an oxygen carrier conversion of 20 %. The conversion of CH_4 generally increased with temperature up to 925 °C, but was slightly lower at 950 °C than at 900 °C. The reason for this observation is not totally clear, but may be related to a lower gas-solid contact time since the total flow rate (at NTP) into the FBR was the same at all temperatures investigated; the effect of the gas-solid contact time was not studied in this work. The ratio of H_2/CO increased with temperature (Fig. 5c) and was greater than the theoretical value of 2, which was unexpected since no carbon deposits were observed when analyzing the reduced (conversion > 70 %) oxygen carrier particles from the FBR using Raman spectroscopy. Further, the carbon balance was poor in the reduction step of the fluidized bed experiments, closing to only ~ 80 %. The remaining ~ 20 % of the carbonaceous gas entering the fluidized bed (i.e. CH_4) may have been deposited as solid carbon, but, again, no evidence of carbon on the surface of the oxygen carrier or in filters was found. This requires further investigations.

The equilibrium ratios of CO/CO_2 or H_2/H_2O (and corresponding conversions of CO_2 or H_2O during oxidation) were determined at the beginning of the mildly exothermic oxidation step with CO_2 or H_2O and are reported in Fig. 5d. The initial peak in CO concentration was due to an overshot in CO_2 flow when opening the gas valve (see blank experiment in Fig. S19 in SI). Using CO_2 as the oxidant, > 96.5 % was converted into CO. The conversion of H_2O to H_2 was > 94 % and was thus slightly lower than the conversion of CO_2 to CO, even though CO_2 and H_2O possess very similar oxidation potentials at the temperatures studied [95]. No significant contamination of the H_2 with CO was observed (Fig. S20 in SI) and the purity of the H_2 was > 99.5 %. The error associated with the measurements of the ratios H_2/H_2O were relatively large as can be seen from the standard deviations in Fig. 5d, which was most likely caused by slight variations in the flow rate of liquid H_2O through the double piston pump that was used in the steam generation part of the reactor setup. Importantly, the ratios of CO/CO_2 or H_2/H_2O were much higher than those observed for most other material compositions that have been employed in CO_2 or H_2O-splitting reaction schemes [95–97].

In the oxidation step with air, a large increase in temperature was observed, although only a little amount of additional lattice oxygen was replenished. The small peak of CO_2 at the beginning of the oxidation reaction was not related to the combustion of carbon deposits, but CO_2 trapped in the manifold that was released when flowing air (see blank experiment in Fig. S19 in SI). We note that an important aspect for the practical use of oxygen carrier particles in high-temperature redox processes (in both FBR and PBR) is their thermal and mechanical stability, which is discussed in Section 2.2 in SI.

3.2.3. Packed bed reactor (PBR)

The third reactor type used in this work was the PBR, in which the stagnant oxygen carrier particles (180–212 µm) reacted from the top (where the gas entered) to the bottom. Reduction was performed in 5 vol.% CH_4/N_2, followed by re-oxidization of the oxygen carrier first in

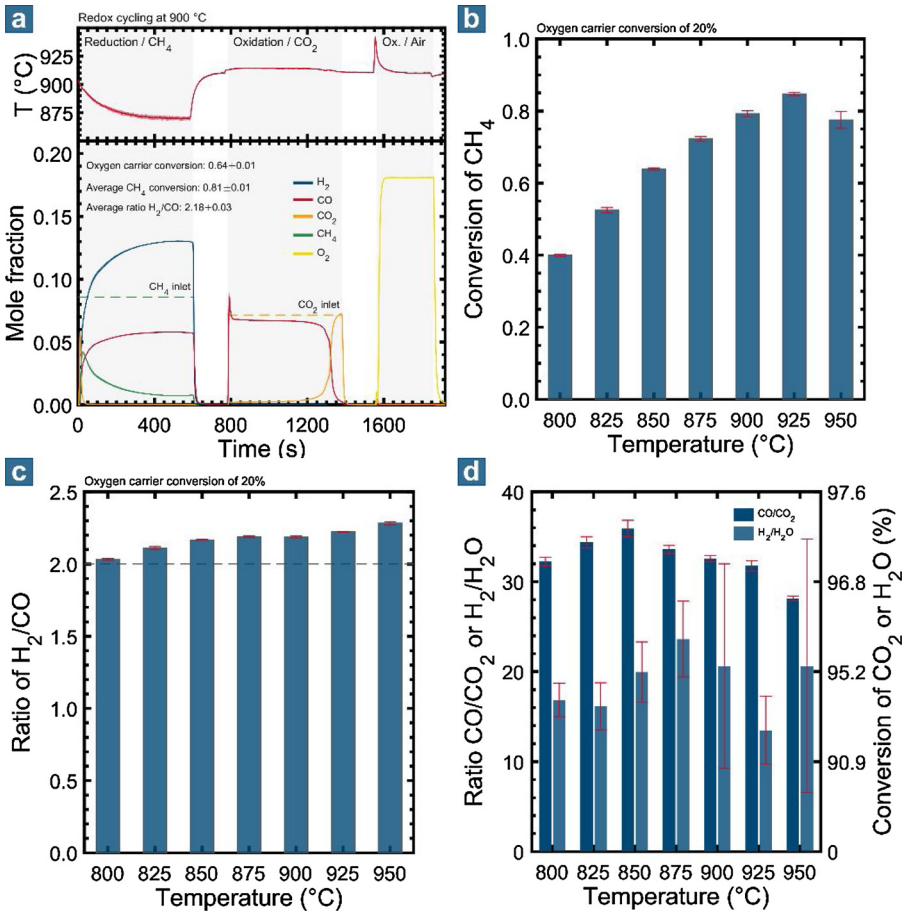

Fig. 5. (a) Average gas concentrations and average bed temperature as a function of time, as measured over at least ten consecutive redox cycles using the FBR with ~ 6.5 g of oxygen carrier particles (355–500 µm) at a set temperature of 900 °C. Error bounds representing two standard deviations are plotted around the averaged curves to illustrate the high cyclic stability. (b) Conversion of CH_4 at an oxygen carrier conversion of 20 % as a function of the set reactor temperature. (c) Ratio of H_2/CO at an oxygen carrier conversion of 20 % as a function of the set reactor temperature. The horizontal grey dashed line indicates the theoretical ratio of 2. (d) Ratio of CO/CO_2 and H_2/H_2O determined at the beginning (after 40 s) of the oxidation step as a function of the set reactor temperature. Error bars in (b), (c) and (d) represent two standard deviation based on measurements over at least ten redox cycles.

5 vol.% CO_2/N_2 and then in 50 vol.% air. Purge steps with pure N_2 (grade 5.0) for 2 min each were performed between the reducing and oxidizing reaction steps for data analysis purposes. Similar to the experiments using the FBR, performance parameters such as conversion of CH_4 are reported for oxygen carrier conversions of 20 %. The conversion of the oxygen carrier was calculated based on the total amount of oxygen carrier loaded into the reactor, but because the oxygen carrier was reduced from top to bottom in the packed bed, local conversions of the oxygen carrier may have been very much different.

At the beginning of the reaction (Fig. 6a, note that O_2 was not measured), CH_4 was converted completely into CO_2 (and H_2O), consistent with the pulse (Fig. 3a,b) and FBR experiments (Fig. 5a). There was then a rapid transition from the total oxidation to the partial oxidation of CH_4 and synthesis gas generation increased with time and conversion of the oxygen carrier. Generally, the conversion of CH_4 was higher in the PBR than in the FBR at a certain reaction temperature (Fig. 6b). The conversion of CH_4 was higher for lower flow rates of gas due to higher gas-solid contact times. At 925 °C, almost all CH_4 was converted into synthesis gas, and so no experiments were performed at 950 °C. The carbon balance closed to within 95 % in the PBR experiments, i.e. much better than in the FBR experiments. The selectivity towards CO was unaffected by the flow rate of CH_4 and decreased with temperature (Fig. 6c), indicating that the decomposition of CH_4 occurred and that carbon was deposited on the oxygen carrier; note that the selectivity towards synthesis gas (CO + H_2) was always > 99 % for oxygen carrier conversions > 3.5 %. The reduction of the oxygen carrier with H_2 or CO (i.e. gas products produced in the top part of the packed bed) was not significant and did not impair the oxygen carrier's high selectivity towards synthesis gas. The ratio of H_2/CO measured during reduction increased with temperature and, surprisingly, was < 2, even though it was apparent that carbon deposition occurred (Fig. 6d). The results shown in Fig. 6d were expected to be seen in the FBR experiments in line with previous work [63], but not in the PBR experiments. We note that H_2 was measured using a thermal conductivity analyzer (ABB, EL3020, Caldos27), which is cross-sensitive towards other gas species, especially CH_4. These cross-sensitivities were accounted for in the calibration of the instrument, and so explaining the results in Fig. 6d requires further investigations. That carbon deposition was significant during reduction can be seen also from the oxidation step with CO_2 in Fig. 6a: The measured concentration of CO was greater than the inlet concentration of CO_2 because, in addition to the re-oxidation of the oxygen carrier (Reaction 3), carbon deposits were gasified (C + CO_2 → 2 CO). The equilibrium ratio of CO/CO_2 was therefore not determined in the PBR experiments. The peak in the concentration of CO at the beginning of the oxidation step with air indicates that not all carbon was gasified with CO_2 in the previous oxidation step (Fig. 6a). We did not observe CO_2 as an oxidation product of deposited carbon when using air in any of the FBR and PBR experiment.

3.3. Part 3 – Continuous synthesis gas production over 45 days

The potential of this oxygen carrier was demonstrated in an experiment over 45 days in the PBR. The oxygen carrier (355–500 µm) was cycled between 5 vol.% CH_4/N_2 and 5 vol.% CO_2/N_2 for 8 min each, using a total flow rate of 50 ml min^{-1} (NTP); one complete redox cycle thus lasted 16 min and more than 4050 redox cycles were performed at an average temperature of 917.7 ± 0.6 °C. The oxygen carrier was mixed with 40 wt% SiC of the same size to avoid blocking of the reactor in case that the particles would disintegrate and form fine powder. There was no additional purge step with pure N_2, nor was air used to re-oxidize the oxygen carrier.

Fig. 7a shows the gas profiles measured during every 500th redox

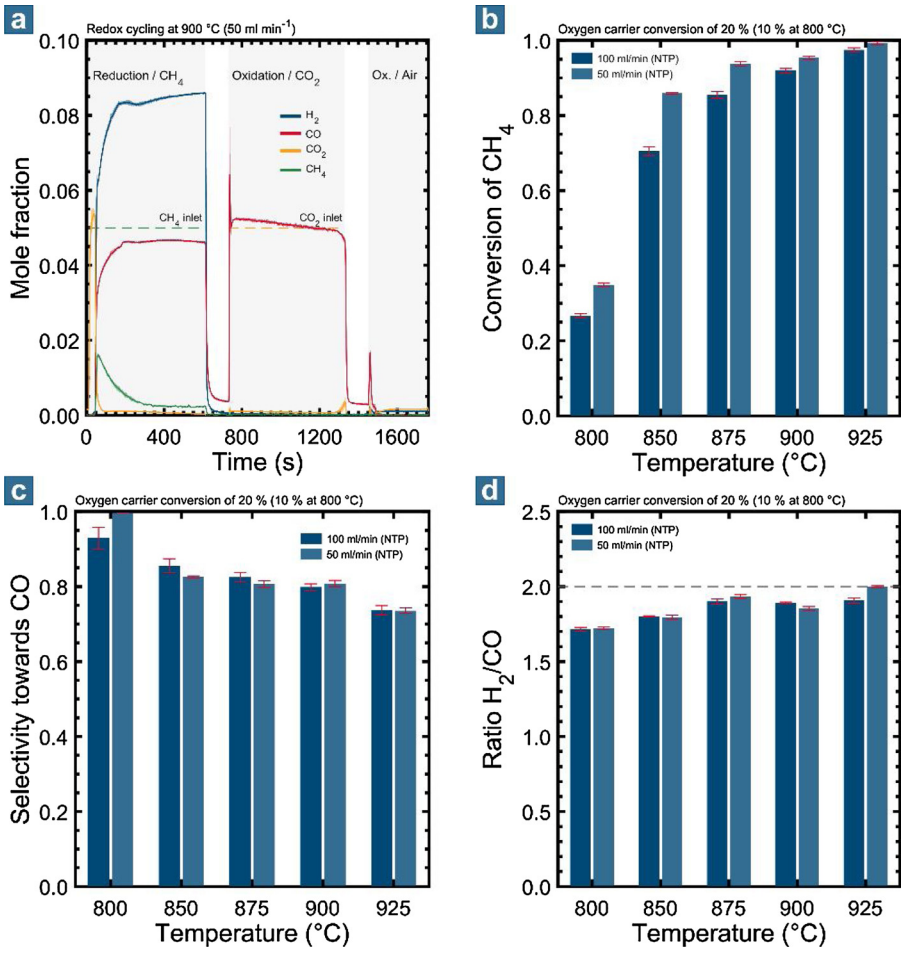

Fig. 6. (a) Average gas concentrations as a function of time, as measured over five consecutive redox cycles using the PBR filled with ~ 1.1 g of oxygen carrier particles (180–212 µm) at a set temperature of 900 °C. Error bounds representing two standard deviations are plotted around the averaged curves to illustrate the high cyclic stability. (b) Conversion of CH_4 at an oxygen carrier conversion of 20 % (10 % at 800 °C) as a function of the set reactor temperature for two different gas flow rates at NTP. (c) Selectivity towards CO at an oxygen carrier conversion of 20 % (10 % at 800 °C) as a function of the set reactor temperature for two different gas flow rates at NTP. (d) Ratio of H_2/CO at an oxygen carrier conversion of 20 % (10 % at 800 °C) as a function of the set reactor temperature for two different gas flow rates at NTP. The horizontal grey dashed line indicates the theoretical ratio of 2. Error bars in (b), (c) and (d) represent two standard deviation based on measurements over at least five redox cycles.

cycle. The concentrations of CH_4 and CO_2 were insignificant, showing that they were converted completely into synthesis gas (Fig. 7b,c); additionally the gas profiles for cycles 1–500 are shown in Fig. S32 in SI. From cycle ~ 100, no significant concentrations of CH_4 or CO_2 were measured. The ratio of H_2/CO during the reduction step increased with cycling (from ~ 2.01–2.55) because increasingly more of the CH_4 entering the reactor was converted into carbon and H_2 than to CO (Fig. 7b,c). Accordingly, the average conversion of the oxygen carrier during reduction decreased from ~ 0.13 to 0.10; the maximum theoretical conversion assuming all CH_4 entering the reactor is partially oxidized was 0.13. The peak in the CO concentration at the beginning of the oxidation step was due to the gasification of carbon deposits with CO_2. If all carbon deposits are gasified in the oxidation step, the average ratio of H_2/CO over an entire redox cycle is one. Here, the ratio of H_2/CO over an entire redox increased from ~ 0.98 to 1.05, implying that carbon accumulated with time and that only some of the carbon was gasified at the beginning of the oxidation step. As was seen also in the TGA experiment towards the end of the 50 redox cycles (Fig. 4e), the re-oxidation of the oxygen carrier was preferred over the oxidation or gasification of carbon when the supply of oxidant was limited. Fig. 7d plots the concentrations of CO and CO_2 at the end of the 45-day experiment; after the last oxidation step, the sample was kept in 5 vol.% CO_2 for another ~ 18 h. The mole fraction of CO in the off-gas was ~ 0.05 for ~ 20 min corresponding to the re-oxidation of the oxygen carrier (Reaction 3) and then increased to ~ 0.074 for ~ 3.5 h due to the gasification of carbon that was either locally separated from the carbon that was gasified at the very beginning of the oxidation step or was more crystalline and thus more resistant to oxidation or gasification. Interestingly, the mole fraction of CO was not ~ 0.095 as the stoichiometry of the gasification reaction with CO_2 would imply ($C + CO_2 \rightarrow 2\,CO$); note that the flow rate of the diluent N_2 was 47.5 ml min^{-1}. This suggests that only roughly half of the CO_2 entering the packed bed was involved in the direct gasification of the carbon. The other half may have been consumed in the replenishment of oxygen vacancies, which would imply that some of the carbon was oxidized through lattice oxygen ($C + [O] \rightarrow CO$) – otherwise the recovery of redox-active lattice oxygen through CO_2 would exceed the oxygen storage capacity by far. Observations made in the PBR experiments in Fig. 6a appear to support this: The CO concentration did not return to zero in the purge steps with N_2, because carbon may have been oxidized by remaining redox-active lattice oxygen, similar to previous results in the context of the dry reforming of CH_4 [98]. The complex interplay of the reactions involved in the oxidation of the carbon deposits seems worth being studied separately. In Fig. 7d all carbon was oxidized when the breakthrough in CO_2 concentration occurred. The mole fractions of CO and CO_2 did not return to, respectively, zero and 0.05 until the furnace was turned off, suggesting a small fraction of the CO_2 was still being converted into CO. The difference to 0.05 in the mole fraction of CO_2 after the furnace was turned off implies a small drift in the calibration of the gas analyzer over the > 45 days of the experiment.

Lastly, the XRD pattern of the collected oxygen carrier showed reflections of Fe_3O_4 as an impurity phase (Fig. 7e). Iron oxide phases separated from the perovskite environment reduce to metallic Fe faster and thus may have contributed to catalyzing the decomposition of CH_4 and reducing the overall reactivity [99]. Results from the in-situ XRD measurements showed that even when Fe_3O_4 was formed, the perovskite structure was readily recovered upon oxidation at temperatures > 800 °C (Fig. 2b/d). However, in the 45-day experiment the oxygen carrier was not re-oxidized completely. Further, we observed via XRD that cementite, an iron carbide (Fe_3C), formed when carbon

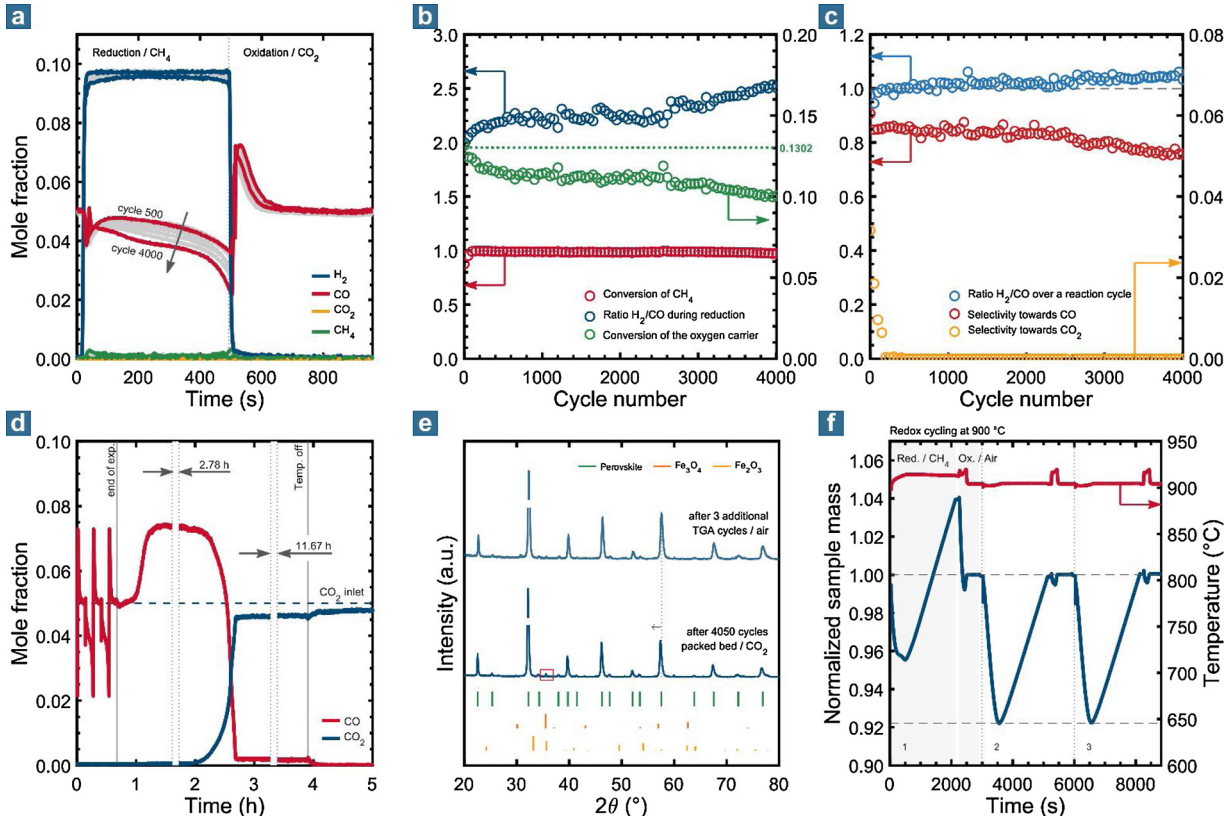

Fig. 7. (a) Measured gas concentrations of every 500th redox cycle plotted as a function of redox cycle time using the PBR with oxygen carrier particles (355–500 µm) mixed with SiC. The grey arrow indicates increasing cycle number. (b) Conversion of CH_4, ratio of H_2/CO and average conversion of the oxygen carrier as a function of cycle number. The horizontal green dashed line indicates the theoretical conversion of the oxygen carrier in one redox cycle assuming all CH_4 is partially oxidized to H_2 and CO. (c) Ratio of H_2/CO over an entire redox cycle, selectivity towards CO and selectivity towards CO_2 as a function of cycle number. (d) Measured gas concentrations of CO and CO_2 plotted as a function of time. The last three redox cycles of the 45-day experiments. Measurements over 2.78 h and 11.67 h were removed from the plot to improve clarity. (e) XRD patterns of the oxygen carrier retrieved from the 45-day experiment and after an additional cycling experiment at 900 °C shown in (f). The red rectangle indicates the position of a reflection due to Fe_3O_4. Reference pattern for Fe_3O_4 and Fe_2O_3 were scaled to their reported intensities to ease comparison with the measurements. (f) Normalized sample mass and temperature of the oxygen carrier retrieved from the 45-day experiment, as measured in the TGA over 3 redox cycles (Reduction in 6.7 vol.% CH_4/N_2, oxidation in 83.3 vol.% air/N_2) (For interpretation of the references to colour in this figure legend, the reader is referred to the web version of this article).

deposition occurred (Fig. S33 in SI), which may have caused the separation of a fraction of the Fe phase from the perovskite environment [100]. The reactivity of the oxygen carrier collected after the long cycling experiment was investigated in the TGA. Fig. 7f shows that the initial reactivity with CH_4 was poor with substantial amounts of carbon deposited during the reduction step analogous to the observations made in the 45-day experiment. After oxidation with air, the oxygen carrier was very reactive again, as can be seen from the rapid decrease in the normalized sample weight in the 2nd and 3rd reduction. Surprisingly, the recovering of the high reactivity was not related to the disappearance of the isolated Fe impurity phase, because it still existed after the experiment (Fig. 7e). Further, TEM/EDX images of the sample before and after the TGA experiment were inconclusive such that a dedicated structural characterization work would be required to understand this observation. The results imply that the oxygen carrier should be regenerated with air from time to time to ensure a cyclically high and stable reactivity.

3.4. Part 4 – process configurations

The results presented in 3.1–3.3 demonstrate the potential of this class of oxygen carrier for the complete conversion of CH_4 to synthesis gas, and the near-complete conversion of the oxidants CO_2 and H_2O to, respectively, CO and H_2. The reduced oxygen carrier is extremely efficient in removing oxidizing species from a gas stream at high temperature (> 800 °C), such that pure streams of e.g. N_2, Ar or He can readily be obtained. If the supply of oxidants is limited, replenishment of lattice oxygen is preferred over the oxidation of carbon. Non-stoichiometric, oxygen-deficient metal oxides that are often used in the context of solar-assisted H_2O/CO_2-splitting or CH_4 reforming display a highly transient behavior in the generation of H_2 and, or, CO, which originates from the change in equilibrium oxygen partial pressure ($p_{O2,eq}$) with δ [101–105]. This is not the case when the metal oxide used as the oxygen carrier undergoes a bulk phase transition at a constant $p_{O2,eq}$, such as the $La_{0.85}Sr_{0.15}Fe_{0.95}Al_{0.05}O_{3-\delta}$ investigated in this work. Upon undergoing a bulk phase transition, a much greater amount of lattice oxygen can be utilized – often an order of magnitude higher compared to materials that supply only non-stoichiometric lattice oxygen that is associated with a change in δ [106,107]. Different from monometallic Fe_2O_3 that reduces in several steps ($Fe_2O_3 \rightarrow Fe_3O_4 \rightarrow FeO \rightarrow Fe$; each phase transition is linked with a different $p_{O2,eq}$ and different reaction products), Fe in a perovskite or brownmillerite environment (e.g. $LaFeO_3$, $SrFeO_3$ [108] or $Ca_2Fe_2O_5$ [95]) reduces to metallic Fe in a single step after non-stoichiometric lattice oxygen from the parent perovskite has been removed. Thus, thermodynamically a constant selectivity towards the partial oxidation products is ensured. Further, Fe_2O_3 requires an inert support material for structural stabilization against sintering [71,109,110], whereas the Fe contained in the perovskite is inherently stabilized through the other components in an orderly environment [111].

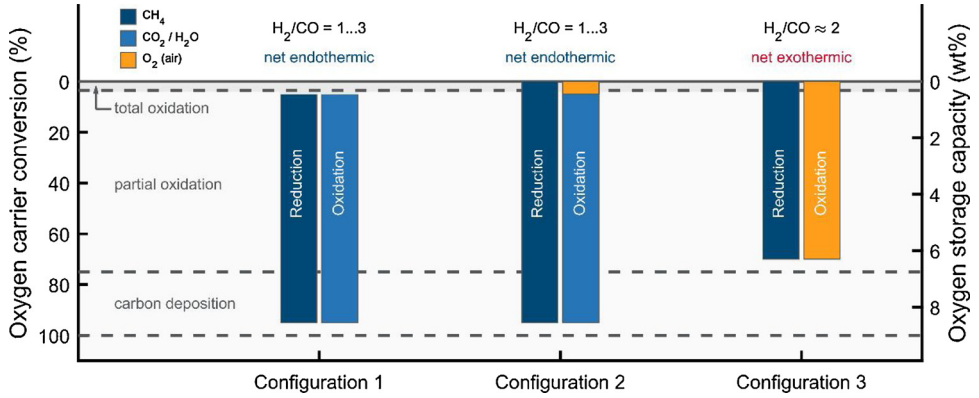

Fig. 8. Overview of potential process configurations using the $La_{0.85}Sr_{0.15}Fe_{0.95}Al_{0.05}O_{3-\delta}$ oxygen carrier.

The chemical and physical properties of $La_{0.85}Sr_{0.15}Fe_{0.95}Al_{0.05}O_{3-\delta}$ offer various interesting process configurations (Fig. 8) that can employ either packed bed or (circulating) fluidized bed reactors. Fluidized beds potentially allow for a uniform reduction of the oxygen carrier such that carbon deposition can be avoided through control of the reduction time (and thus the degree of reduction). Upon oxidation with H_2O, H_2 free of carbon contaminants (CO_x) can be produced.

3.4.1. Configuration 1 for synthesis gas / CO / H_2

The entire two-step process aims at producing synthesis gas without CO_2 contamination. In the reduction step, CH_4 is converted into synthesis gas. In the oxidation step, CO and, or, H_2 are produced. The ratio of H_2/CO can be adjusted through the choice of the oxidant, CO_2, H_2O or both (from 1:1 to 3:1) and thus be made suitable for different downstream conversion processes. If carbon deposition occurs during reduction, these carbon deposits are gasified with CO_2 and, or, H_2O, in the oxidation step, so that the net effect over an entire reaction cycle is the same as if no carbon deposition had happened. The process also allows for removing separately the product gases produced in the respective reduction and oxidation steps, i.e. synthesis gas (reduction step), and CO or H_2 or synthesis gas (oxidation step). Nearly pure CO can readily be produced from the splitting of CO_2, whereas the purity of the H_2 (when using H_2O as the oxidant) depends on the amount of carbon deposited in the previous reduction step. The simultaneous gasification of carbon deposits when using CO_2 in the oxidation step enables its full conversion, whereas in the absence of carbon deposits, the conversion of CO_2 is ~ 97 % in a mixed reactor (Fig. 5d). The exothermicity of the oxidation step is lowered according to the extent of the carbon deposition/gasification. There is no need for a separate supply of air or O_2 in this process configuration. Heat integration is problematic owing to the strongly endothermic reduction reaction, similar to the DRM and SRM reactions. Recent works have demonstrated the potential of solar reactors as means to supply thermal energy and replace fossil fuel combustion [112,113].

3.4.2. Configuration 2 for synthesis gas (flexible ratio H_2/CO) with CO_2 and heat

Through altering the composition of the oxygen carrier, its oxygen transfer properties can be adjusted: Increasing the substitution of La^{3+} by Sr^{2+} increases the oxidation state of the Fe and so enables for a higher oxygen storage capacity selective for the exothermic total oxidation of CH_4 [63]. In the reduction step, synthesis gas containing CO_2 is produced, which may be desirable for methanol production using commercial $Cu/ZnO/Al_2O_3$ catalysts [114–116]. In the oxidation reaction with CO and, or, H_2, the ratio of H_2/CO is adjusted to match the requirements of the synthesis gas for further processing. A third reaction step with air regenerates the oxygen carrier and produces heat that can be utilized within the process.

3.4.3. Configuration 3 for synthesis gas (fixed ratio H_2/CO) with CO_2 and heat

In a two-step process, the reduction with CH_4 produces synthesis gas with a ratio of H_2/CO ≈ 2 and small amounts of CO_2. The oxidation step is performed with air, thereby producing heat that can be utilized to drive the endothermic reduction. The entire redox cycle is exothermic and would thus permit autothermal operation. The extent of reduction of the oxygen carrier should be limited to avoid (i) excessive sintering during its re-oxidation, and (ii) the oxidation of carbon deposits, which would be released to the atmosphere with the air stream.

4. Conclusions

In our work we highlight the potential of $LaFeO_3$-based oxygen carriers, specifically $La_{0.85}Sr_{0.15}Fe_{0.95}Al_{0.05}O_{3-\delta}$, for the partial oxidation of CH_4 to synthesis gas and the splitting of CO_2 and H_2O to CO and H_2, respectively. The oxygen carrier was investigated in depth and its cyclic redox performance assessed in different types of reactors. The oxygen carrier underwent a bulk phase transition in a single, extended step, which ensured a high selectivity towards the partial oxidation products and a high oxygen storage capacity of ~ 9 wt%. We demonstrate that over a period of more than 45 days (≈ 4050 redox cycles), CH_4 and CO_2, two greenhouse gases, were converted completely into synthesis gas with a ratio of H_2/CO ≈ 1 in a packed bed reactor; higher H_2/CO ratios up to 3 are feasible if H_2O is used as the oxidant instead of CO_2. This has been the longest continuous operation of an oxygen carrier at high temperature in the area of chemical looping thus far. Results of preliminary experiments performed at 10 bar suggest that the partial oxidation and splitting reactions are feasible also at elevated pressure and yield similar conversions and selectivities.

The compositional flexibility of the oxygen carrier offers potential for further material optimization. Avoiding carbon deposition will not be possible if metallic Fe forms during the reduction reaction owing to its catalytic promotion of the decomposition of CH_4. Important will be the successful operation at high pressure (up to 50 bar) such that the oxygen carrier-mediated “reforming” of CH_4 can become a serious alternative to established industrial processes [117].

Credit author statement

F.D. conceived and designed the experiments. F.D. performed the experiments (if not stated otherwise in the acknowledgement section) and analyzed the data. F.D. wrote the manuscript. C.M. guided the project and contributed to the writing of the paper.

Declaration of Competing Interest

The authors declare that they have no known competing financial interests or personal relationships that could have appeared to

influence the work reported in this paper.

Acknowledgements

The work is part of “GaSTech” project under the Horizon 2020 programme, ACT Grant Agreement No. 691712, and we acknowledge financial support by the Swiss Federal Office of Energy and the European Commission. We thank Dr. Knuth Albertsen and Geert van Diest from Euro Support Advanced Materials B.V. for providing the metal oxide powder. We thank Dr. Agnieszka Kierzkowska for conducting the microscoping work (both SEM and TEM) and Athanasia Tsoukalou for conducting the XPS measurements. We are grateful to Dr. Paula M. Abdala for helping with the Rietveld refinement of XRD data. We thank Dr. Sung Min Kim for assisting with the pulse experiments. The Scientific Centre for Optical and Electron Microscopy (ScopeM) at ETH Zürich is acknowledged for providing training on and access to electron microscopes and the Laboratory of Surface Science and Technology at ETH Zürich for granting access to their XPS facilities.

Appendix A. Supplementary data

Supplementary material related to this article can be found, in the online version, at doi:https://doi.org/10.1016/j.apcatb.2020.119328.

References

[1] X. Zhu, Q. Imtiaz, F. Donat, C.R. Müller, F. Li, Chemical looping beyond combustion – a perspective, Energy Environ. Sci. 13 (2020) 772–804, https://doi.org/10.1039/C9EE03793D.
[2] L. Zeng, Z. Cheng, J.A. Fan, L.-S. Fan, J. Gong, Metal oxide redox chemistry for chemical looping processes, Int. Rev. Chem. Eng. 2 (2018) 349–364, https://doi.org/10.1038/s41570-018-0046-2.
[3] Q. Zhang, J. Kang, Y. Wang, Development of novel catalysts for Fischer–tropsch synthesis: tuning the product selectivity, ChemCatChem. 2 (2010) 1030–1058, https://doi.org/10.1002/cctc.201000071.
[4] S. Abelló, D. Montané, Exploring iron-based multifunctional catalysts for Fischer–Tropsch synthesis: a review, ChemSusChem. 4 (2011) 1538–1556, https://doi.org/10.1002/cssc.201100189.
[5] F. Ausfelder, A. Bazzanella, Hydrogen in the chemical industry, Hydrog. Sci. Eng. Mater. Process. Syst. Technol. (2016) 19–40, https://doi.org/10.1002/9783527674268.ch02.
[6] X. Jiang, X. Nie, X. Guo, C. Song, J.G. Chen, Recent advances in carbon dioxide hydrogenation to methanol via heterogeneous catalysis, Chem. Rev. (2020), https://doi.org/10.1021/acs.chemrev.9b00723.
[7] M. Fathi, E. Bjorgum, T. Viig, O. Rokstad, Partial oxidation of methane to synthesis gas: elimination of gas phase oxygen, Catal. Today 63 (2000) 489–497, https://doi.org/10.1016/S0920-5861(00)00495-8.
[8] A. Lyngfelt, C. Linderholm, Chemical-looping combustion of solid fuels – status and recent progress, Energy Procedia 114 (2017) 371–386, https://doi.org/10.1016/j.egypro.2017.03.1179.
[9] J. Adánez, A. Abad, T. Mendiara, P. Gayán, L.F. de Diego, F. García-Labiano, Chemical looping combustion of solid fuels, Prog. Energy Combust. Sci. 65 (2018) 6–66, https://doi.org/10.1016/j.pecs.2017.07.005.
[10] J. Adánez, A. Abad, Chemical-looping combustion: status and research needs, Proc. Combust. Inst. 37 (2019) 4303–4317, https://doi.org/10.1016/j.proci.2018.09.002.
[11] F. Donat, W. Hu, S.A. Scott, J.S. Dennis, Characteristics of copper-based oxygen carriers supported on calcium aluminates for chemical-looping combustion with oxygen uncoupling (CLOU), Ind. Eng. Chem. Res. 54 (2015), https://doi.org/10.1021/acs.iecr.5b01172.
[12] X. Zhu, K. Li, L. Neal, F. Li, Perovskites as geo-inspired oxygen storage materials for chemical looping and three-way catalysis: a perspective, ACS Catal. 8 (2018) 8213–8236, https://doi.org/10.1021/acscatal.8b01973.
[13] S.G. Nadgouda, M. Guo, A. Tong, L.-S. Fan, High purity syngas and hydrogen coproduction using copper-iron oxygen carriers in chemical looping reforming process, Appl. Energy 235 (2019) 1415–1426, https://doi.org/10.1016/j.apenergy.2018.11.051.
[14] C. Park, T.-L. Hsieh, Y. Pottimurthy, V. Shah, D. Xu, Y.-Y. Chen, L.-S. Fan, A. Tong, Design and operations of a 15 kWth subpilot unit for the methane-to-Syngas chemical looping process with CO_2 utilization, Ind. Eng. Chem. Res. 59 (2020) 6886–6899, https://doi.org/10.1021/acs.iecr.9b05577.
[15] S. Luo, L. Zeng, D. Xu, M. Kathe, E. Chung, N. Deshpande, L. Qin, A. Majumder, T.-L. Hsieh, A. Tong, Z. Sun, L.-S. Fan, Shale gas-to-syngas chemical looping process for stable shale gas conversion to high purity syngas with a H$\$n 2$\$n : CO ratio of 2 : 1, Energy Environ. Sci. 7 (2014) 4104–4117, https://doi.org/10.1039/C4EE02892A.
[16] Y. Liu, L. Qin, Z. Cheng, J.W. Goetze, F. Kong, J.A. Fan, L.-S. Fan, Near 100% CO selectivity in nanoscaled iron-based oxygen carriers for chemical looping methane partial oxidation, Nat. Commun. 10 (2019) 5503, https://doi.org/10.1038/s41467-019-13560-0.
[17] Y. Kang, M. Tian, C. Huang, J. Lin, B. Hou, X. Pan, L. Li, A.I. Rykov, J. Wang, X. Wang, Improving syngas selectivity of Fe2O3/Al2O3 with yttrium modification in chemical looping methane conversion, ACS Catal. 9 (2019) 8373–8382, https://doi.org/10.1021/acscatal.9b02730.
[18] M. Guo, Z. Cheng, Y. Liu, L. Qin, J. Goetze, J.A. Fan, L.-S. Fan, Cobalt doping modification for enhanced methane conversion at low temperature in chemical looping reforming systems, Catal. Today (2019), https://doi.org/10.1016/j.cattod.2019.06.016.
[19] S. Zhang, Y. Wan, Z. Xu, S. Xue, L. Zhang, B. Zhang, C. Xia, Bismuth doped La0.75Sr0.25Cr0.5Mn0.5O3-δ perovskite as novel redox-stable efficient anode for solid oxide fuel cell, J. Mater. Chem. A (2020), https://doi.org/10.1039/D0TA03328F.
[20] S.S. Hashim, F. Liang, W. Zhou, J. Sunarso, Cobalt-free perovskite cathodes for solid oxide fuel cells, ChemElectroChem. 6 (2019) 3549–3569, https://doi.org/10.1002/celc.201900391.
[21] E. Olsson, J. Cottom, X. Aparicio-Anglès, N.H. de Leeuw, Computational study of the mixed B-site perovskite SmBxCo1 − xO3 − d (B = Mn, Fe, Ni, Cu) for next generation solid oxide fuel cell cathodes, Phys. Chem. Chem. Phys. 21 (2019) 9407–9418, https://doi.org/10.1039/C9CP00995G.
[22] F. Lu, T. Xia, Q. Li, J. Wang, L. Huo, H. Zhao, Heterostructured simple perovskite nanorod-decorated double perovskite cathode for solid oxide fuel cells: highly catalytic activity, stability and CO2-durability for oxygen reduction reaction, Appl. Catal. B Environ. 249 (2019) 19–31, https://doi.org/10.1016/j.apcatb.2019.02.056.
[23] Z. Liu, K. Li, H. Zhao, K. Świerczek, High-performance oxygen permeation membranes: cobalt-free Ba0.975La0.025Fe1-xCuxO3-δ ceramics, J. Mater. 5 (2019) 264–272, https://doi.org/10.1016/j.jmat.2019.01.013.
[24] J. Gao, Y. Lun, N. Han, X. Tan, C. Fan, S. Liu, Influence of nitric oxide on the oxygen permeation behavior of La0.6Sr0.4Co0.2Fe0.8O3 − δ perovskite membranes, Sep. Purif. Technol. 210 (2019) 900–906, https://doi.org/10.1016/j.seppur.2018.09.001.
[25] R. Ruhl, J. Song, V. Thoréton, S.P. Singh, K. Wiik, Y. Larring, H.J.M. Bouwmeester, Structure, electrical conductivity and oxygen transport properties of perovskite-type oxides CaMn1 − x − yTixFeyO3 − δ, Phys. Chem. Chem. Phys. 21 (2019) 21824–21835, https://doi.org/10.1039/C9CP04911H.
[26] A.A. Alharbi, A. Sackmann, U. Weimar, N. Bârsan, Acetylene- and ethylene-sensing mechanism for LaFeO3-Based gas sensors: operando insights, J. Phys. Chem. C 124 (2020) 7317–7326, https://doi.org/10.1021/acs.jpcc.0c01052.
[27] K. Yang, J. Ma, X. Qiao, Y. Cui, L. Jia, H. Wang, Hierarchical porous LaFeO3 nanostructure for efficient trace detection of formaldehyde, Sensors Actuators B Chem. 313 (2020) 128022, , https://doi.org/10.1016/j.snb.2020.128022.
[28] M. Chen, H. Wang, J. Hu, Y. Zhang, K. Li, D. Zhang, S. Zhou, J. Zhang, Z. Zhu, Q. Liu, Near-room-Temperature ethanol gas sensor based on mesoporous Ag/Zn–LaFeO3 nanocomposite, Adv. Mater. Interfaces 6 (2019) 1801453, https://doi.org/10.1002/admi.201801453.
[29] S. Gong, Z. Xie, W. Li, X. Wu, N. Han, Y. Chen, Highly active and humidity resistive perovskite LaFeO3 based catalysts for efficient ozone decomposition, Appl. Catal. B Environ. 241 (2019) 578–587, https://doi.org/10.1016/j.apcatb.2018.09.041.
[30] K. Tamai, S. Hosokawa, H. Okamoto, H. Asakura, K. Teramura, T. Tanaka, NOx oxidation and storage properties of a ruddlesden–Popper-Type Sr3Fe2O7 − δ-Layered perovskite catalyst, ACS Appl. Mater. Interfaces 11 (2019) 26985–26993, https://doi.org/10.1021/acsami.9b08139.
[31] W.-J. Yin, B. Weng, J. Ge, Q. Sun, Z. Li, Y. Yan, Oxide perovskites, double perovskites and derivatives for electrocatalysis, photocatalysis, and photovoltaics, Energy Environ. Sci. 12 (2019) 442–462, https://doi.org/10.1039/C8EE01574K.
[32] Q. Ji, L. Bi, J. Zhang, H. Cao, X.S. Zhao, The role of oxygen vacancies of ABO3 perovskite oxides in the oxygen reduction reaction, Energy Environ. Sci. (2020), https://doi.org/10.1039/D0EE00092B.
[33] D. Li, R. Xu, Z. Gu, X. Zhu, S. Qing, K. Li, Chemical-looping conversion of methane: a review, Energy Technol. (2019) 1900925, https://doi.org/10.1002/ente.201900925 n/a.
[34] D. Li, R. Xu, X. Li, Z. Li, X. Zhu, K. Li, Chemical looping conversion of gaseous and liquid fuels for chemical production: a review, Energy Fuels (2020), https://doi.org/10.1021/acs.energyfuels.0c01006.
[35] C. Huang, J. Wu, Y.-T. Chen, M. Tian, A.I. Rykov, B. Hou, J. Lin, C.-R. Chang, X. Pan, J. Wang, A. Wang, X. Wang, In situ encapsulation of iron(0) for solar thermochemical syngas production over iron-based perovskite material, Commun. Chem. 1 (2018) 55, https://doi.org/10.1038/s42004-018-0050-y.
[36] T. Jia, Z. Zeng, X. Zhang, P. Ohodnicki, B. Chorpening, G. Hackett, J. Lekse, Y. Duan, The influence of oxygen vacancy on the electronic and optical properties of ABO3 − δ (A = La, Sr, B = Fe, Co) perovskites, Phys. Chem. Chem. Phys. 21 (2019) 20454–20462, https://doi.org/10.1039/C9CP03883C.
[37] A.B. Muñoz-García, A.M. Ritzmann, M. Pavone, J.A. Keith, E.A. Carter, Oxygen transport in perovskite-type solid oxide fuel cell materials: insights from quantum mechanics, Acc. Chem. Res. 47 (2014) 3340–3348, https://doi.org/10.1021/ar4003174.
[38] Y.-S. Zheng, M. Zhang, Q. Li, Y.-A. Zhu, Z.-J. Sui, D. Chen, X.-G. Zhou, Electronic origin of oxygen transport behavior in La-Based perovskites: a density functional theory study, J. Phys. Chem. C 123 (2019) 275–290, https://doi.org/10.1021/acs.jpcc.8b11249.
[39] H. Chang, E. Bjørgum, O. Mihai, J. Yang, H.L. Lein, T. Grande, S. Raaen, Y.-A. Zhu, A. Holmen, D. Chen, Effects of oxygen mobility in La–Fe-based perovskites on the catalytic activity and selectivity of methane oxidation, ACS Catal. 10 (2020) 3707–3719, https://doi.org/10.1021/acscatal.9b05154.

[40] Q. Li, Y.-X. Deng, Y.-A. Zhu, Y. Li, Z.-J. Sui, D. Chen, W.-K. Yuan, Structural stability of Lanthanum-based oxygen-deficient perovskites in redox catalysis: a density functional theory study, Catal. Today (2018), https://doi.org/10.1016/j.cattod.2018.04.070.
[41] A.A. Emery, J.E. Saal, S. Kirklin, V.I. Hegde, C. Wolverton, High-throughput computational screening of perovskites for thermochemical water splitting applications, Chem. Mater. 28 (2016) 5621–5634, https://doi.org/10.1021/acs.chemmater.6b01182.
[42] F. Martinez-Ortega, C. Batiot-Dupeyrat, G. Valderrama, J.-M. Tatibouët, Methane catalytic combustion on La-based perovskite catalysts, Comptes Rendus l'Académie Des Sci. - Ser. IIC - Chem. 4 (2001) 49–55, https://doi.org/10.1016/S1387-1609(00)01202-0.
[43] T. Seiyama, Total oxidation of hydrocarbons on perovskite oxides, Catal. Rev. 34 (1992) 281–300, https://doi.org/10.1080/01614949208016313.
[44] M. Alifanti, J. Kirchnerova, B. Delmon, Effect of substitution by cerium on the activity of LaMnO3 perovskite in methane combustion, Appl. Catal. A Gen. 245 (2003) 231–244, https://doi.org/10.1016/S0926-860X(02)00644-0.
[45] O. Mihai, D. Chen, A. Holmen, Catalytic consequence of oxygen of lanthanum ferrite perovskite in chemical looping reforming of methane, Ind. Eng. Chem. Res. 50 (2011) 2613–2621, https://doi.org/10.1021/ie100651d.
[46] A.M. Ritzmann, A.B. Muñoz-García, M. Pavone, J.A. Keith, E.A. Carter, Ab Initio DFT + U analysis of oxygen vacancy formation and migration in La1-xSrxFeO3-δ (x = 0, 0.25, 0.50), Chem. Mater. 25 (2013) 3011–3019, https://doi.org/10.1021/cm401052w.
[47] F.H. Taylor, J. Buckeridge, C.R.A. Catlow, Screening divalent metals for a- and B-Site dopants in LaFeO3, Chem. Mater. 29 (2017) 8147–8157, https://doi.org/10.1021/acs.chemmater.7b01993.
[48] D.D. Taylor, N.J. Schreiber, B.D. Levitas, W. Xu, P.S. Whitfield, E.E. Rodriguez, Oxygen storage properties of La1–xSrxFeO3 − δ for chemical-looping reactions—an in situ neutron and synchrotron X-ray study, Chem. Mater. 28 (2016) 3951–3960, https://doi.org/10.1021/acs.chemmater.6b01274.
[49] A. Jones, M.S. Islam, Atomic-scale insight into LaFeO3 perovskite: defect nanoclusters and ion migration, J. Phys. Chem. C 112 (2008) 4455–4462, https://doi.org/10.1021/jp710463x.
[50] F. He, J. Chen, S. Liu, Z. Huang, G. Wei, G. Wang, Y. Cao, K. Zhao, La1-xSrxFeO3 perovskite-type oxides for chemical-looping steam methane reforming: identification of the surface elements and redox cyclic performance, Int. J. Hydrogen Energy 44 (2019) 10265–10276, https://doi.org/10.1016/J.IJHYDENE.2019.03.002.
[51] R.B. da Silva, J.M. Soares, J.A.P. da Costa, J.H. de Araújo, A.R. Rodrigues, F.L.A. Machado, Local iron ion distribution and magnetic properties of the perovskites La1-xSrxFeO3-γ, J. Magn. Magn. Mater. 466 (2018) 306–310, https://doi.org/10.1016/j.jmmm.2018.07.040.
[52] A. Bayon, A. de la Calle, K.K. Ghose, A. Page, R. McNaughton, Experimental, computational and thermodynamic studies in perovskites metal oxides for thermochemical fuel production: a review, Int. J. Hydrogen Energy 45 (2020) 12653–12679, https://doi.org/10.1016/j.ijhydene.2020.02.126.
[53] J. Song, D. Ning, H.J.M. Bouwmeester, Influence of alkaline-earth metal substitution on structure, electrical conductivity and oxygen transport properties of perovskite-type oxides La0.6A0.4FeO3-δ (A = Ca, Sr and Ba), Phys. Chem. Chem. Phys. (2020), https://doi.org/10.1039/D0CP00247J.
[54] J. Mizusaki, M. Yoshihiro, S. Yamauchi, K. Fueki, Nonstoichiometry and defect structure of the perovskite-type oxides La1-xSrxFeO3-˚, J. Solid State Chem. 58 (1985) 257–266, https://doi.org/10.1016/0022-4596(85)90243-9.
[55] G. Luongo, F. Donat, C.R. Müller, Structural and thermodynamic study of Ca A- or Co B-site substituted SrFeO3-δ perovskites for low temperature chemical looping applications, Phys. Chem. Chem. Phys. (2020).
[56] J. Vieten, B. Bulfin, P. Huck, M. Horton, D. Guban, L. Zhu, Y. Lu, K.A. Persson, M. Roeb, C. Sattler, Materials design of perovskite solid solutions for thermochemical applications, Energy Environ. Sci. 12 (2019) 1369–1384, https://doi.org/10.1039/c9ee00085b.
[57] D. Sastre, D.P. Serrano, P. Pizarro, J.M. Coronado, Chemical insights on the activity of La1-xSrxFeO3 perovskites for chemical looping reforming of methane coupled with CO_2-splitting, J. CO2 Util. 31 (2019) 16–26, https://doi.org/10.1016/J.JCOU.2019.02.013.
[58] R.-J. Li, C.-C. Yu, W.-J. Ji, S.-K. Shen, Methane oxidation to synthesis gas using lattice oxygen in La1 − xSrxFeO3 perovskite oxides instead of molecular oxygen, Stud. Surf. Sci. Catal. 147 (2004) 199–204, https://doi.org/10.1016/S0167-2991(04)80051-X.
[59] L.M. Neal, A. Shafiefarhood, F. Li, Dynamic methane partial oxidation using a Fe2O3@La0.8Sr0.2FeO3-δ core–shell redox catalyst in the absence of gaseous oxygen, ACS Catal. 4 (2014) 3560–3569, https://doi.org/10.1021/cs5008415.
[60] L. Neal, A. Shafiefarhood, F. Li, Effect of core and shell compositions on MeOx@LaySr1 − yFeO3 core–shell redox catalysts for chemical looping reforming of methane, Appl. Energy 157 (2015) 391–398, https://doi.org/10.1016/j.apenergy.2015.06.028.
[61] Y. Chen, X. Zhu, K. Li, Y. Wei, Y. Zheng, H. Wang, Chemical looping co-splitting of H2O-CO_2 for efficient generation of syngas, ACS Sustain. Chem. Eng. 7 (2019) 15452–15462, https://doi.org/10.1021/acssuschemeng.9b02996.
[62] H. Ding, Y. Xu, C. Luo, Q. Wang, C. Shen, J. Xu, L. Zhang, A novel composite perovskite-based material for chemical-looping steam methane reforming to hydrogen and syngas, Energy Convers. Manage. 171 (2018) 12–19, https://doi.org/10.1016/j.enconman.2018.05.088.
[63] F. Donat, Y. Xu, C.R. Müller, Combined partial oxidation of methane to synthesis gas and production of hydrogen or carbon monoxide in a fluidized bed using lattice oxygen, Energy Technol. (2019).
[64] F. Donat, Y. Xu, C.R. Müller, Combined partial oxidation of methane to synthesis gas and production of hydrogen or carbon monoxide in a fluidized bed using lattice oxygen, Energy Technol. (2019), https://doi.org/10.1002/ente.201900655.
[65] G. Greczynski, L. Hultman, X-ray photoelectron spectroscopy: towards reliable binding energy referencing, Prog. Mater. Sci. 107 (2020) 100591, , https://doi.org/10.1016/j.pmatsci.2019.100591.
[66] T. Mattisson, J. Adánez, K. Mayer, F. Snijkers, G. Williams, E. Wesker, O. Bertsch, A. Lyngfelt, Innovative oxygen carriers uplifting chemical-looping combustion, Energy Procedia 63 (2014) 113–130, https://doi.org/10.1016/j.egypro.2014.11.012.
[67] A. Abad, A. Cabello, P. Gayán, F. García-Labiano, L.F. de Diego, T. Mendiara, J. Adánez, Kinetics of CaMn0.775Ti0.125Mg0.1O2.9-δ perovskite prepared at industrial scale and its implication on the performance of chemical looping combustion of methane, Chem. Eng. J. 394 (2020) 124863, , https://doi.org/10.1016/j.cej.2020.124863.
[68] R.H. Görke, E.J. Marek, F. Donat, S.A. Scott, Reduction and oxidation behavior of strontium perovskites for chemical looping air separation, Int. J. Greenh. Gas Control. 94 (2020) 102891, , https://doi.org/10.1016/j.ijggc.2019.102891.
[69] W. Hu, F. Donat, S.A. Scott, J.S. Dennis, Kinetics of oxygen uncoupling of a copper based oxygen carrier, Appl. Energy 161 (2016) 92–100, https://doi.org/10.1016/j.apenergy.2015.10.006.
[70] W. Hu, E. Marek, F. Donat, J.S. Dennis, S.A. Scott, A thermogravimetric method for the measurement of CO/CO2 ratio at the surface of carbon during combustion, Proc. Combust. Inst. 37 (2019) 2987–2993, https://doi.org/10.1016/J.PROCI.2018.05.040.
[71] D. Hosseini, F. Donat, S.M. Kim, L. Bernard, A.M. Kierzkowska, C.R. Müller, Redox-driven restructuring of FeMnZr-Oxygen carriers enhances the purity and yield of H2 in a chemical looping process, ACS appl. Energy Mater. 1 (2018) 1294–1303, https://doi.org/10.1021/acsaem.8b00023.
[72] A.J. Jennings, S.J. Skinner, Ö. Helgason, Structural properties of LaxSr2 − xFeO4 ± δ at high temperature and under reducing conditions, J. Solid State Chem. 175 (2003) 207–217, https://doi.org/10.1016/S0022-4596(03)00248-2.
[73] T. Li, R.S. Jayathilake, D.D. Taylor, E.E. Rodriguez, Structural studies of the perovskite series La1 − xSrxCoO3 − δ during chemical looping with methane, Chem. Commun. (Camb.) 55 (2019) 4929–4932, https://doi.org/10.1039/C8CC09573F.
[74] M. Ouyang, P. Boldrin, R.C. Maher, X. Chen, X. Liu, L.F. Cohen, N.P. Brandon, A mechanistic study of the interactions between methane and nickel supported on doped ceria, Appl. Catal. B Environ. 248 (2019) 332–340, https://doi.org/10.1016/j.apcatb.2019.02.038.
[75] Y. Zheng, K. Li, H. Wang, D. Tian, Y. Wang, X. Zhu, Y. Wei, M. Zheng, Y. Luo, Designed oxygen carriers from macroporous LaFeO3 supported CeO2 for chemical-looping reforming of methane, Appl. Catal. B Environ. 202 (2017) 51–63, https://doi.org/10.1016/j.apcatb.2016.08.024.
[76] A. Shafiefarhood, J.C. Hamill, L.M. Neal, F. Li, Methane partial oxidation using FeOx@La0.8Sr0.2FeO3-[small delta] core-shell catalyst - transient pulse studies, Phys. Chem. Chem. Phys. 17 (2015) 31297–31307, https://doi.org/10.1039/C5CP05583K.
[77] A. Shafiefarhood, J. Zhang, L.M. Neal, F. Li, Rh-promoted mixed oxides for "low-temperature" methane partial oxidation in the absence of gaseous oxidants, J. Mater. Chem. A Mater. Energy Sustain. 5 (2017) 11930–11939, https://doi.org/10.1039/C7TA01398A.
[78] J. Haber, W. Turek, Kinetic studies as a method to differentiate between oxygen species involved in the oxidation of Propene, J. Catal. 190 (2000) 320–326, https://doi.org/10.1006/jcat.1999.2764.
[79] V.V. Kaichev, V.I. Bukhtiyarov, M. Hävecker, A. Knop-Gercke, R.W. Mayer, R. Schlögl, The nature of Electrophilic and nucleophilic oxygen adsorbed on silver, React. Kinet. Catal. Lett. 44 (2003) 432–440, https://doi.org/10.1023/A:1024459305551.
[80] R. Zhang, Y. Cao, H. Li, Z. Zhao, K. Zhao, L. Jiang, The role of CuO modified La0·7Sr0·3FeO3 perovskite on intermediate-temperature partial oxidation of methane via chemical looping scheme, Int. J. Hydrogen Energy 45 (2020) 4073–4083, https://doi.org/10.1016/j.ijhydene.2019.12.082.
[81] K. Zhao, A. Zheng, H. Li, F. He, Z. Huang, G. Wei, Y. Shen, Z. Zhao, Exploration of the mechanism of chemical looping steam methane reforming using double perovskite-type oxides La1.6Sr0.4FeCoO6, Appl. Catal. B Environ. 219 (2017) 672–682, https://doi.org/10.1016/j.apcatb.2017.08.027.
[82] X. Shen, Y. Sun, Y. Wu, J. Wang, E. Jiang, X. Xu, J. Su, Z. Jia, The coupling of CH4 partial oxidation and CO2 splitting for syngas production via double perovskite-type oxides LaFexCo1 − xO3, Fuel 268 (2020) 117381, https://doi.org/10.1016/j.fuel.2020.117381.
[83] Thermo Scientific, Thermo Scientifc XPS Reference Table of Elements, (n.d.). https://xpssimplified.com/.
[84] T. Yamashita, P. Hayes, Analysis of XPS spectra of Fe2+ and Fe3+ ions in oxide materials, Appl. Surf. Sci. 254 (2008) 2441–2449, https://doi.org/10.1016/j.apsusc.2007.09.063.
[85] B. Kucharczyk, J. Okal, W. Tylus, J. Winiarski, B. Szczygieł, The effect of the calcination temperature of LaFeO3 precursors on the properties and catalytic activity of perovskite in methane oxidation, Ceram. Int. 45 (2019) 2779–2788, https://doi.org/10.1016/j.ceramint.2018.07.299.
[86] B. Klingenberg, M.A. Vannice, Influence of pretreatment on lanthanum nitrate, carbonate, and oxide powders, Chem. Mater. 8 (1996) 2755–2768, https://doi.org/10.1021/cm9602555.
[87] A.C. Ferrari, J. Robertson, Raman spectroscopy of amorphous, nanostructured, diamond-like carbon, and nanodiamond, Philos. Trans. R. Soc. A Math. Phys. Eng.

Sci. 362 (2004) 2477–2512, https://doi.org/10.1098/rsta.2004.1452.
[88] D.S. Knight, W.B. White, Characterization of diamond films by Raman spectroscopy, J. Mater. Res. 4 (1989) 385–393, https://doi.org/10.1557/JMR.1989.0385.
[89] N.D. Charisiou, S.L. Douvartzides, G.I. Siakavelas, L. Tzounis, V. Sebastian, V. Stolojan, S.J. Hinder, M.A. Baker, K. Polychronopoulou, M.A. Goula, The relationship between reaction temperature and carbon deposition on nickel catalysts based on Al2O3, ZrO2 or SiO2 supports during the biogas dry reforming reaction, Catalysts 9 (2019), https://doi.org/10.3390/catal9080676.
[90] C. Palmer, D.C. Upham, S. Smart, M.J. Gordon, H. Metiu, E.W. McFarland, Dry reforming of methane catalysed by molten metal alloys, Nat. Catal. 3 (2020) 83–89, https://doi.org/10.1038/s41929-019-0416-2.
[91] M. Rydén, A. Lyngfelt, T. Mattisson, D. Chen, A. Holmen, E. Bjørgum, Novel oxygen-carrier materials for chemical-looping combustion and chemical-looping reforming; LaxSr1 − xFeyCo1 − yO3 − $δ$ perovskites and mixed-metal oxides of NiO, Fe2O3 and Mn3O4, Int. J. Greenh. Gas Control. 2 (2008) 21–36, https://doi.org/10.1016/S1750-5836(07)00107-7.
[92] X. Dai, C. Yu, R. Li, Q. Wu, K. Shi, Z. Hao, Effect of calcination temperature and reaction conditions on methane partial oxidation using lanthanum-based perovskite as oxygen donor, J. Rare Earths. 26 (2008) 341–346, https://doi.org/10.1016/S1002-0721(08)60092-7.
[93] Z. Cheng, L. Qin, M. Guo, M. Xu, J.A. Fan, L.-S. Fan, Oxygen vacancy promoted methane partial oxidation over iron oxide oxygen carriers in the chemical looping process, Phys. Chem. Chem. Phys. 18 (2016) 32418–32428, https://doi.org/10.1039/C6CP06264D.
[94] L. Qin, M. Guo, Y. Liu, Z. Cheng, J.A. Fan, L.-S. Fan, Enhanced methane conversion in chemical looping partial oxidation systems using a copper doping modification, Appl. Catal. B Environ. 235 (2018) 143–149, https://doi.org/10.1016/j.apcatb.2018.04.072.
[95] D. Hosseini, F. Donat, P.M. Abdala, S.M. Kim, A.M. Kierzkowska, C.R. Müller, Reversible exsolution of dopant improves the performance of Ca2Fe2O5 for chemical looping hydrogen production, ACS Appl. Mater. Interfaces 11 (2019) 18276–18284, https://doi.org/10.1021/acsami.8b16732.
[96] M.S.C. Chan, W. Liu, M. Ismail, Y. Yang, S.A. Scott, J.S. Dennis, Improving hydrogen yields, and hydrogen:steam ratio in the chemical looping production of hydrogen using Ca2Fe2O5, Chem. Eng. J. 296 (2016) 406–411, https://doi.org/10.1016/j.cej.2016.03.132.
[97] H.V. Pralhad, H. Feng, M. Amit, L. Fanxing, Iron-doped BaMnO3 for hybrid water splitting and syngas generation, ChemSusChem. 10 (2017) 3282, https://doi.org/10.1002/cssc.201701620.
[98] S.M. Kim, P.M. Abdala, T. Margossian, D. Hosseini, L. Foppa, A. Armutlulu, W. van Beek, A. Comas-Vives, C. Copéret, C. Müller, Cooperativity and dynamics increase the performance of NiFe dry reforming catalysts, J. Am. Chem. Soc. 139 (2017) 1937–1949, https://doi.org/10.1021/jacs.6b11487.
[99] J. Faye, A. Baylet, M. Trentesaux, S. Royer, F. Dumeignil, D. Duprez, S. Valange, J.-M. Tatibouët, Influence of lanthanum stoichiometry in La1 − xFeO3 − δ perovskites on their structure and catalytic performance in CH4 total oxidation, Appl. Catal. B Environ. 126 (2012) 134–143, https://doi.org/10.1016/j.apcatb.2012.07.001.
[100] S. Geng, W. Ding, S. Guo, X. Zou, Y. Zhang, X. Lu, Carbon deposition on iron surfaces in CO-CO2 atmosphere, Ironmak. Steelmak. 42 (2015) 714–720, https://doi.org/10.1179/1743281215Y.0000000049.
[101] A.J. Carrillo, K.J. Kim, Z.D. Hood, A.H. Bork, J.L.M. Rupp, La0.6Sr0.4Cr0.8Co0.2O3 perovskite decorated with exsolved Co nanoparticles for stable CO2 splitting and syngas production, ACS Appl. Energy Mater. (2020), https://doi.org/10.1021/acsaem.0c00249.
[102] D. Marxer, P. Furler, M. Takacs, A. Steinfeld, Solar thermochemical splitting of CO2 into separate streams of CO and O2 with high selectivity, stability, conversion, and efficiency, Energy Environ. Sci. 10 (2017) 1142–1149, https://doi.org/10.1039/C6EE03776C.
[103] M. Kubicek, A.H. Bork, J.L.M. Rupp, Perovskite oxides-a review on a versatile material class for solar-to-fuel conversion processes, J. Mater. Chem. A 5 (2017) 11983–12000, https://doi.org/10.1039/c7ta00987a.
[104] S. Ackermann, L. Sauvin, R. Castiglioni, J.L.M. Rupp, J.R. Scheffe, A. Steinfeld, Kinetics of CO_2 reduction over nonstoichiometric ceria, J. Phys. Chem. C 119 (2015) 16452–16461, https://doi.org/10.1021/acs.jpcc.5b03464.
[105] A. Haeussler, S. Abanades, A. Julbe, J. Jouannaux, M. Drobek, A. Ayral, B. Cartoixa, Remarkable performance of microstructured ceria foams for thermochemical splitting of H2O and CO2 in a novel high–temperature solar reactor, Chem. Eng. Res. Des. 156 (2020) 311–323, https://doi.org/10.1016/j.cherd.2020.02.008.
[106] I.S. Metcalfe, B. Ray, C. Dejoie, W. Hu, C. de Leeuwe, C. Dueso, F.R. García-García, C.-M. Mak, E.I. Papaioannou, C.R. Thompson, J.S.O. Evans, Overcoming chemical equilibrium limitations using a thermodynamically reversible chemical reactor, Nat. Chem. (2019), https://doi.org/10.1038/s41557-019-0273-2.
[107] J. Zhang, V. Haribal, F. Li, Perovskite nanocomposites as effective CO&sub&2& /sub&-splitting agents in a cyclic redox scheme, Sci. Adv. 3 (2017) e1701184, https://doi.org/10.1126/sciadv.1701184.
[108] E. Marek, W. Hu, M. Gaultois, C.P. Grey, S.A. Scott, The use of strontium ferrite in chemical looping systems, Appl. Energy 223 (2018) 369–382, https://doi.org/10.1016/J.APENERGY.2018.04.090.
[109] D. Hosseini, P.M. Abdala, F. Donat, S.M. Kim, C.R. Müller, Bifunctional core-shell architecture allows stable H2 production utilizing CH4 and CO_2 in a catalytic chemical looping process, Appl. Catal. B Environ. 258 (2019) 117946, , https://doi.org/10.1016/j.apcatb.2019.117946.
[110] C. Chung, L. Qin, V. Shah, L.-S. Fan, Chemically and physically robust, commercially-viable iron-based composite oxygen carriers sustainable over 3000 redox cycles at high temperatures for chemical looping applications, Energy Environ. Sci. 10 (2017) 2318–2323, https://doi.org/10.1039/C7EE02657A.
[111] O. Mihai, D. Chen, A. Holmen, Chemical looping methane partial oxidation: the effect of the crystal size and O content of LaFeO 3, J. Catal. 293 (2012) 175–185, https://doi.org/10.1016/j.jcat.2012.06.022.
[112] K.J. Warren, R.J. Carrillo, B. Greek, C.M. Hill, J.R. Scheffe, Solar reactor demonstration of efficient and selective syngas production via chemical-looping dry reforming of methane over Ceria, Energy Technol. (2020) 2000053, https://doi.org/10.1002/ente.202000053 n/a.
[113] J.R. Fosheim, B.J. Hathaway, J.H. Davidson, High efficiency solar chemical-looping methane reforming with ceria in a fixed-bed reactor, Energy 169 (2019) 597–612, https://doi.org/10.1016/j.energy.2018.12.037.
[114] K.M.V. Bussche, G.F. Froment, A steady-state kinetic model for methanol synthesis and the water gas shift reaction on a commercial Cu/ZnO/Al2O3Catalyst, J. Catal. 161 (1996) 1–10, https://doi.org/10.1006/jcat.1996.0156.
[115] K.G. Chanchlani, R.R. Hudgins, P.L. Silveston, Methanol synthesis from H2, CO, and C02 over Cu/ZnO catalysts, J. Catal. 136 (1992) 59–75, https://doi.org/10.1016/0021-9517(92)90106-R.
[116] A. González-Garay, M.S. Frei, A. Al-Qahtani, C. Mondelli, G. Guillén-Gosálbez, J. Pérez-Ramírez, Plant-to-planet analysis of CO2-based methanol processes, Energy Environ. Sci. 12 (2019) 3425–3436, https://doi.org/10.1039/C9EE01673B.
[117] A. Ramirez, J. Gascon, Support was the key to success, Joule 4 (2020) 714–716, https://doi.org/10.1016/j.joule.2020.03.009.